Three-dimensional numerical investigation of a suspension flow in an eccentric Couette flow geometry

A. Badia, E. d'Ambrosio, Y. d'Angelo, F. Peters, L. Lobry

Three-dimensional numerical investigation of a suspension flow in an eccentric Couette flow geometry

A. Badia,[1,2] E. D'Ambrosio,[2] Y. D'Angelo,[1] F. Peters,[2] and L. Lobry[2]
[1)]*Université Côte d'Azur, Laboratoire Mathématiques & Interactions J.A. Dieudonné, LJAD, UMR 7351 CNRS, Nice, France*
[2)]*Université Côte d'Azur, Institut de Physique de Nice, InPhyNi, UMR 7010 CNRS, Nice, France*

(*Electronic mail: Laurent.Lobry@univ-cotedazur.fr)

(Dated: 11 January 2024)

This paper investigates the influence of eccentricity on flow characteristics and particle migration in Couette geometries. The study involves numerical simulations using the recent frame-invariant model developed by Badia *et al.* [1]. The study begins with a two-dimensional analysis, focusing first on Newtonian fluid, in order to thoroughly characterize the specific properties of this flow configuration. Next, the impact of eccentricity on particle migration in an isodense suspension is examined by numerical simulations based on the experiments conducted by Subia *et al.* [2]. Furthermore, the study is extended to include a full three-dimensional analysis of a dense suspension flow in an eccentric Couette geometry, based on resuspension experiments conducted by Saint-Michel *et al.* [3] and D'Ambrosio, Blanc, and Lemaire [4]. The main objective of the latter study is to investigate the influence of eccentricity on the resuspension height and on the calculation of the particle normal stress in the vertical direction through volume fraction profile analysis. Our results show that even minimal eccentricity can lead to significant changes compared to the centered case.

I. INTRODUCTION

Whether in the industrial sector or in the natural sciences, the description of flows involving suspensions requires an advanced understanding of the mechanisms operating in such complex flows. Depending on the geometry and the type of suspension, various complex physical phenomena, coupled or not, may be involved.

Cylindrical Couette geometry is one of the most commonly used devices for studying and understanding the behavior of suspensions. Since the first work of Gadala-Maria [5], it is known that for such a geometry, a concentrated isodense suspension undergoes particle migration. The rotation of the inner cylinder of a Couette cell containing a uniform suspension generates particle migration towards the outer cylinder, where the shear rate is the lowest. Several experimental[6–10], numerical[1,2,11–13] and even analytical works[9,14,15] have been carried out to study and measure such particle migration.

Similarly, when an initially sedimented dense particle suspension is sheared in a cylindrical Couette cell, vertical motion of the particles is induced until a non-uniform stationary vertical concentration distribution is reached. This phenomenon, called viscous resuspension, is the result of the balance between a downward flow of particles due to gravity and an upward flow of particles induced by shear[16]. Several papers in the literature have addressed this problem. Indeed, Acrivos, Mauri, and Fan [17] studied viscous resuspension by both analytically establishing the vertical concentration profile and experimentally measuring the resuspension height.

Particle migration and viscous resuspension share the same theoretical framework. We give here a short account on the literature concerning the modeling of particle migration. Detailed historical reviews can be found in other sources[18–20]. The simplest theoretical description of particle migration, and the first from a historical perspective, is based on a phenomenological diffusion equation, where the diffusion flux is related to the shear rate and volume fraction gradients[6,9]. Despite its simplicity and suitability for computational studies, Denn and Morris [18] noted conflicts with experiments in geometries beyond the Couette cell. Then Nott and Brady [14] introduced the Suspension Balance Model (SBM) to explain the migration observed in their particle resolved simulations of a channel flow. Starting from the momentum balance equation for the particle phase, they identified the divergence of a particle stress as the driving force that induces the particle flux. In the considered (parallel) channel flow, the stress anisotropy was not relevant. Taking the stress anisotropy into account is mandatory when curvilinear geometries are involved. The SBM was reformulated by Morris and Boulay [15] to this purpose, allowing to generalize the SBM to account for flow and migration in the main rheometrical flows. This reformulation was confirmed by experiments by Dbouk, Lobry, and Lemaire [21]. Later, a frame-invariant formulation for the stresses was proposed to tackle general flows, mainly 2D, as opposed to quasi-simple-shear flows[22]. Finally, the SBM was revisited in order to discuss in depth the nature of the driving stress[23,24].

As highlighted above, a precise knowledge of the suspension rheology is of primary importance in order to tackle suspension flows, including migration and resuspension. A huge amount of experimental, theoretical and numerical work has been devoted to the characterization of the suspension rheology and its relation to the relevant particle scale mecanisms, including hydrodynamic interactions and contact forces. The interested reader is referred to recent reviews for detailed information[18,19,25,26]. One of the main issues is the anisotropic rheological behaviour of such suspensions. Experimental characterization of the full stress tensor has been undertaken for a long time[21,27–29]. The contribution of R.Tanner and co-workers in that field is of primary importance, in particular concerning the experimental determination of the relevant material functions in shear[30,31] or elongational flow[32],

including their rate dependence[33] and their relation to the particle surface roughness[34]. In addition, they recently proposed a general tensorial formulation of the stress constitutive laws for non-Brownian suspensions[35] inspired from polymer material rheology, which model is close to the one used in the following.

Modeling stress anisotropy in general suspension flow is not an easy task. Some models explicitly accounts for the shear-induced microstructure, often modeled using a time varying tensor field. Such models are able to tackle even complex flows with reasonable accuracy, including shear-reversal[36–38], superposition of steady and perpendicular oscillatory shear[39] and shear rotation[40], with the drawback though that they are sometimes difficult to calibrate. Some models follows a simpler approach, as in the present paper, where no explicit reference to the microstructure is included[1,35,41]. Such models are simpler, but cannot tackle fast transient flows like shear-reversal.

Regarding the particle stress responsible for migration and resuspension, experimental determination have been carried out too[21,42]. The work by Zarraga, Hill, and Leighton [27] or those, more recent, by Saint-Michel *et al.* [3] and by D'Ambrosio, Blanc, and Lemaire [4,43] deal with the determination of the normal stress in the vorticity direction from experimental measurements of the solid concentration profile. It should be noted that very few studies dealing with discrete numerical simulations of this problem can be found in the literature[44]. Other papers deal with particle resuspension in the direction of the velocity gradient[45], in particular in the frame of bedload transport[46].

The flow of a Newtonian fluid between two eccentric cylinders has been widely studied, both theoretically and numerically. One of the important features of this flow is the development of a recirculation zone when the eccentricity exceeds a threshold value[47,48], leading to additional mixing effects[49]. Subia *et al.* [2] propose a short bibliography where several theoretical and numerical papers on the topic are listed. If a rich literature is available, which deals with the flow of a Newtonian fluid in an eccentric Couette geometry, or with the suspension flow in a centered Couette geometry, the situation is quite different concerning the suspension flow in an eccentric Couette geometry. Among the few studies available in the literature, we can mention the articles by Phan-Thien *et al.* [50] and by Subia *et al.* [2] who numerically and experimentally studied the flow of an isodense suspension for two different values of the eccentricity. However, to our knowledge, the case of a suspension of dense particles has not been tackled in the past.

In the present paper, we make use of numerical simulation to study in detail the flow of non-Brownian suspensions in an eccentric Couette geometry. To this aim, we use the frame-invariant model recently developed and validated by Badia *et al.* [1]. In the frame of this three-dimensional model, close to the SBM, the driving force for particle migration originates in the divergence of the contact contribution to the stress. All stresses are computed from frame-invariant constitutive laws taking into account the anisotropic normal stresses and allowing the simulation of quasi-stationary suspension flows in general geometries. Such constitutive laws share similarities with second-order fluid modeling, a well-established concept in polymer rheology[51,52]. Its adaptation to suspension flow problems is very close to that proposed by Lhuillier [23] and, as mentioned above, by Mahmud, Dai, and Tanner [35]. This model makes it possible to study numerically flows that are more complex than conventional rheometric flows, and which are found in industrial applications such as journal bearings.

In section II, we recall the equations of the frame-invariant model developed by Badia *et al.* [1]. Section III presents a study of the two-dimensional (2D) flow in an eccentric Couette geometry, starting with a Newtonian fluid as an introduction. In a second part, we will be interested in the influence of the eccentricity on particle migration in an isodense suspension through the simulation of the experiments by Subia *et al.* [2]. Finally, section IV deals with the three-dimensional (3D) eccentric Couette flow of a dense suspension. This study is based on the resuspension experiments by Saint-Michel *et al.* [3] and by D'Ambrosio, Blanc, and Lemaire [4].

II. MATHEMATICAL MODELING

In a previous work[1], we proposed a numerical modelling suitable for any quasi-steady state suspension flow in general geometry. This model, developed and validated numerically on several kinds of flow, is a version of the SBM, which is based on a continuous single-phase approach, derived from a two-phase modelling. The stress tensors are expressed via a frame-invariant formulation allowing the simulation of any type of quasi-steady flow. Below are recalled the modelling equations that we consider.

The suspension, modelled here as a continuous medium, consists of rigid spherical particles of radius a and density ρ_p suspended in a Newtonian fluid of viscosity η_f and density ρ_f. The main constitutive equations, i.e. continuity, momentum and particulate phase continuity equations, can be expressed as follows:

$$\boldsymbol{\nabla}.\mathbf{u} = 0 \tag{1a}$$

$$\frac{\partial \rho_m \mathbf{u}}{\partial t} + \boldsymbol{\nabla}.(\rho_m \mathbf{u} \otimes \mathbf{u}) = \boldsymbol{\nabla}.\boldsymbol{\Sigma} + \rho_m \mathbf{g} \tag{1b}$$

$$\frac{\partial \phi}{\partial t} + \boldsymbol{\nabla}.(\phi \mathbf{u}) + \boldsymbol{\nabla}.(\phi \mathbf{u}_{sed}) = -\boldsymbol{\nabla}.\mathbf{J}_{migr} \tag{1c}$$

Here, ϕ denotes the volume fraction of particles, $\mathbf{u}$ and ρ_m are the average velocity and density of the mixture defined as $\mathbf{u} = \phi \mathbf{v}_p + (1-\phi)\mathbf{v}_f$, $\rho_m = \phi\rho_p + (1-\phi)\rho_f$, where $\mathbf{v}_p$ and $\mathbf{v}_f$ are respectively the underlying particle and fluid phase velocity field. $\boldsymbol{\Sigma}$ is the total stress of the suspension defined as $\boldsymbol{\Sigma} = \boldsymbol{\Sigma}^f + \boldsymbol{\Sigma}^c$, with $\boldsymbol{\Sigma}^f$ the fluid stress tensor and $\boldsymbol{\Sigma}^c$ the particle contact stress tensor. $\mathbf{g}$ is the gravitational acceleration.

$\boldsymbol{u}_{sed}$ is the sedimentation velocity corrected for the suspension acceleration:

$$\boldsymbol{u}_{sed} = \frac{2a^2 f(\phi)}{9\eta_f}\left((\rho_p - \rho_f)\left[\mathbf{g} - \frac{D\mathbf{u}}{Dt}\right]\right) \tag{2}$$

where $f(\phi) = (1-\phi)^{5.1}$ is the empirical hindered settling function.
$\boldsymbol{J}_{migr}$ is the migration flux of particles originating from the presence of contact forces between particles :

$$\mathbf{J}_{migr} = \frac{2a^2 f(\phi)}{9\eta_f} \boldsymbol{\nabla}.\boldsymbol{\Sigma}^c \tag{3}$$

where $\boldsymbol{\Sigma}^c$ stands for the direct contribution of the contact forces to the stress, with no hydrodynamic contribution. The choice of $\boldsymbol{\Sigma}^c$ as the driving stress for particle migration deserves a few words. In the pioneering version of the SBM, the particle stress including the fluid particle interaction contribution was selected[14,15,53]. Later, Lhuillier[23] and Nott, Guazzelli, and Pouliquen[24] showed that the relevant stress primarily originates in the contact force contribution, possibly supplemented by some hydrodynamic contribution though. In the present modeling, the simplest version of the SBM is chosen.

This system of equation is closed by giving a frame-invariant expression for the total and contact stress tensors[1]:

$$\begin{aligned}\boldsymbol{\Sigma} = &-p\mathbf{I} + \eta_f\eta_s\dot{\gamma}\big(2\hat{\mathbf{E}} \\ &+2\left(\hat{N}_1+2\hat{N}_2\right)\left(\hat{\mathbf{E}}.\hat{\mathbf{E}} - \frac{tr(\hat{\mathbf{E}}.\hat{\mathbf{E}})}{3}\mathbf{I}\right) - \hat{N}_1\frac{1}{\dot{\gamma}}\frac{\mathscr{D}\hat{\mathbf{E}}}{\mathscr{D}t}\Big)\end{aligned} \tag{4a}$$

$$\begin{aligned}\boldsymbol{\Sigma}^c = &\eta_f\eta_s\dot{\gamma}\Big(\hat{\Sigma}^c_{33}\mathbf{I} + 2\frac{\eta_c}{\eta_s}\hat{\mathbf{E}} \\ &+4\left(\frac{\hat{\Sigma}^c_{11}+\hat{\Sigma}^c_{22}}{2} - \hat{\Sigma}^c_{33}\right)\hat{\mathbf{E}}.\hat{\mathbf{E}} - \left(\hat{\Sigma}^c_{11}-\hat{\Sigma}^c_{22}\right)\frac{1}{\dot{\gamma}}\frac{\mathscr{D}\hat{\mathbf{E}}}{\mathscr{D}t}\Big)\end{aligned} \tag{4b}$$

where p is the average fluid pressure, $\mathbf{I}$ is identity, $\hat{\mathbf{E}} = \mathbf{E}/\dot{\gamma}$ is the reduced deformation rate tensor and $\dot{\gamma} = \sqrt{2\mathbf{E}:\mathbf{E}}$ is the shear rate; $\mathscr{D}\hat{\mathbf{E}}/\mathscr{D}t$ denotes the Jaumann derivative, defined as:

$$\frac{\mathscr{D}\hat{\mathbf{E}}}{\mathscr{D}t} = \frac{\partial\hat{\mathbf{E}}}{\partial t} + (\mathbf{u}.\boldsymbol{\nabla})\hat{\mathbf{E}} + \hat{\mathbf{E}}.\boldsymbol{\Omega} - \boldsymbol{\Omega}.\hat{\mathbf{E}} \tag{5}$$

with $\boldsymbol{\Omega}$ the vorticity tensor. Since we deal here with quasi-steady state flows, the term $\partial\hat{\mathbf{E}}/\partial t$ can be omitted. Parameters η_s, η_c, $\hat{N}_i = N_i/(\eta_f\eta_s\dot{\gamma})$ and $\hat{\Sigma}^c_{ii} = \Sigma^c_{ii}/(\eta_f\eta_s\dot{\gamma})$ are functions of ϕ and denote respectively the effective viscosity, the contact viscosity, the normalized normal stress differences ($N_1 = \Sigma_{11}-\Sigma_{22}$ and $N_2 = \Sigma_{22}-\Sigma_{33}$) and the normal contact stresses in simple shear flow. The reader is referred to Badia *et al.*[1] for detailed expressions of these parameters, which have been determined from particle scale simulations[54–56]. It's worth noting again that Mahmud, Dai, and Tanner[35] (please also refer to the paper by Tanner[25]) have recently formulated a frame-invariant constitutive relation, closely similar to the expression found in equation (4a), to calculate the total stress.

Eqs. 4 and 5 deserve a few comments. A detailed discussion may be found in Badia *et al.*[1]. Focusing on Eq. 4b and leaving aside the pressure term, the third and fourth term inside the parenthesis induce normal stress differences in homogeneous simple shear flow. This is easily understood in the case of the third term, which depends on the squared reduced deformation rate tensor $\hat{\mathbf{E}}$. The fourth term is responsible for the first normal stress differences as measured in simple shear flow. In homogeneous simple shear flow, and in steady concentric cylindrical Couette flow, the Jaumann derivative involves the difference between the angular velocity of the eigenframe of $\hat{\mathbf{E}}$, $\boldsymbol{\Omega}_{\boldsymbol{E}}$[51], and the fluid angular velocity, $\boldsymbol{\Omega}$:

$$\frac{\mathscr{D}\hat{\mathbf{E}}}{\mathscr{D}t} = (\boldsymbol{\Omega}_{\boldsymbol{E}}-\boldsymbol{\Omega})\cdot\hat{\mathbf{E}} - \hat{\mathbf{E}}\cdot(\boldsymbol{\Omega}_{\boldsymbol{E}}-\boldsymbol{\Omega}) \tag{6}$$

In homogeneous shear flow and in concentric cylindrical Couette flow, $\|\boldsymbol{\Omega}_{\boldsymbol{E}}-\boldsymbol{\Omega}\| = \dot{\gamma}/2$ and Eq. 4 with Eq. 5 yields the same expression for the stresses as the usual formulation in simple shear flow, in the flow-aligned frame $(\mathbf{v}, \boldsymbol{\nabla}\mathbf{v}, \boldsymbol{\nabla}\times\mathbf{v})$. As an example, in the case of the centered cylindrical Couette flow, the contact stress tensors writes in the azimuthal reference frame $(\mathbf{e}_r, \mathbf{e}_\theta, \mathbf{e}_z)$:

$$\begin{aligned}\boldsymbol{\Sigma}^c &= 2\eta_f\eta_c\mathbf{E} \\ &+ \eta_f\eta_s\dot{\gamma}\left[\hat{\Sigma}^c_{33}\mathbf{I} + \left(\frac{\hat{\Sigma}^c_{11}+\hat{\Sigma}^c_{22}}{2} - \hat{\Sigma}^c_{33}\right)\begin{pmatrix}1&0&0\\0&1&0\\0&0&0\end{pmatrix}\right. \\ &\left. - \frac{\hat{\Sigma}^c_{22}-\hat{\Sigma}^c_{11}}{2}\begin{pmatrix}-1&0&0\\0&1&0\\0&0&0\end{pmatrix}\right] \\ &= 2\eta_f\eta_c\mathbf{E} + \eta_f\eta_s\dot{\gamma}\begin{pmatrix}\hat{\Sigma}^c_{22}&0&0\\0&\hat{\Sigma}^c_{11}&0\\0&0&\hat{\Sigma}^c_{33}\end{pmatrix}\end{aligned} \tag{7}$$

As discussed by Badia *et al.*[1], the present frame-invariant formulation allows computation of the stress tensor when the flow field is locally very different from a standard simple shear flow, i.e. when the flow-aligned tensor model is difficult to use, in particular in 2D flows when $\|\boldsymbol{\Omega}_E - \boldsymbol{\Omega}\| \ll \dot{\gamma}/2$ (extensional flow) or $\|\boldsymbol{\Omega}_E - \boldsymbol{\Omega}\| \gg \dot{\gamma}/2$ (solid body rotation). The interested reader is referred to Badia *et al.*[1] for an in-depth discussion, and to Badia[57] for a comparison with the 2D frame-invariant model proposed by Miller, Singh, and Morris[22].

The numerical resolution of the system of equations (1) is performed by making use of the popular open source software package OpenFOAM. OpenFOAM is a C++ Computational Fluid Dynamics toolbox that uses the finite volume method on a colocated grid for the discretization of the partial differential equations system. Again, we refer to the paper by Badia *et al.*[1] for a detailed presentation of the algorithm and discretization schemes used. It should be noted that in the present work we use an *upwind-downwind* discretization scheme for the term related to sedimentation flux in equation (1c)[58,59]. This scheme guarantees the solution for a problem with discontinuous flux to be bounded.

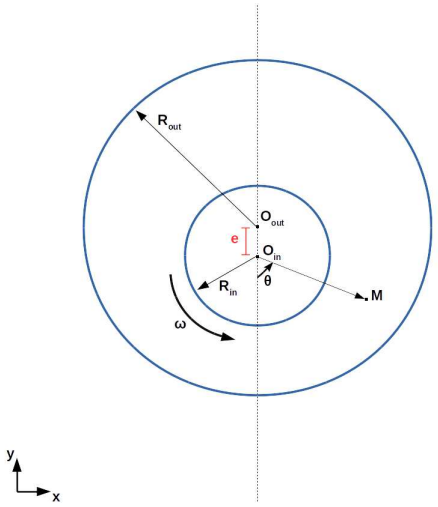

FIG. 1. Sketch of the eccentric Couette geometry

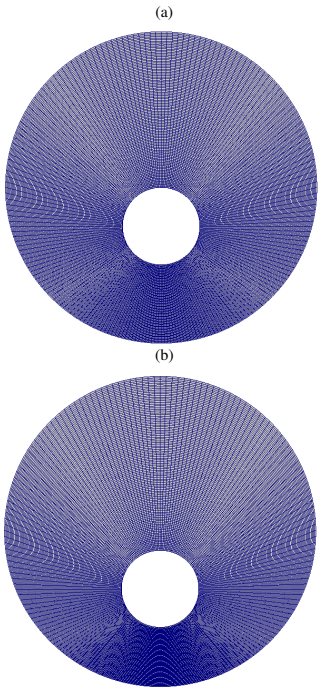

FIG. 2. 2*D* computational mesh for the eccentric Couette geometry: 100 meshes in the radial direction and 200 meshes in the azimuthal direction. (a) $\varepsilon = 1/3$ (b) $\varepsilon = 1/2$.

III. TWO-DIMENSIONAL ECCENTRIC COUETTE FLOW

A. Newtonian fluid

The flow of a Newtonian fluid in an eccentric Couette geometry, i.e. when the axes of the inner and outer cylinders are parallel but not merged, has been widely studied, both theoretically and numerically. One of the well-known features of this flow is the development of a recirculation zone for a sufficiently large eccentricity. A first approach to solve this problem analytically is the lubrication approximation[60]. However, this method is limited to cylinders with nearly equal radii. Another approach, more elaborate, is that of Wannier[47] who proposes an analytical solution by solving biharmonic equations for the stream function. We refer to the paper by Subia *et al.*[2] for a brief bibliography on this topic.

Throughout the present work, the outer cylinder, centered at O_{out} and of radius R_{out}, is stationary, while the inner cylinder, centered at O_{in} and of radius R_{in}, rotates at an angular velocity ω (see Fig. 1). The distance between the respective parallel axes is denoted by e and the eccentricity ratio ε is defined as $\varepsilon = e/(R_{out} - R_{in})$. The origin of the reference frame $(\mathbf{e}_x, \mathbf{e}_y)$ is the center of the inner cylinder O_{in}. Let M be any point located between the two cylinders. As shown in Fig. 1, θ defines the angle formed by the segment $O_{in}M$ and the axis $-\mathbf{e}_y$. We consider for the time being that the cylinders are infinite so that the flow is invariant in the $\mathbf{E}_z$ direction, and takes place in the plane orthogonal to the cylinders axes.

First, we want to calculate the velocity and pressure associated with this flow. The geometry studied is that of Subia *et al.*[2], i.e. cylinders of radius $R_{in} = 6.4$ *mm*, $R_{out} = 25.4$ *mm* and for two values of the eccentricity ratio $\varepsilon = 1/3$, $\varepsilon = 1/2$. This first study is performed for a small Reynolds number $Re = (R_{out} - R_{in})R_{in}\omega\rho_f/\eta_f \approx 0.039$. The numerical mesh is 2*D* with 100 meshes in the radial direction and 200 meshes in the azimuthal direction, see Fig. 2. Regarding the boundary conditions, an angular velocity is imposed on the inner cylinder while a no-slip condition is imposed on the outer cylinder. Please refer to[1] for the boundary conditions applied to the other variables.

In Fig. 3, the pressure at the outer cylinder obtained from the numerical simulation is plotted as a function of angle θ for all two values of the eccentricity and compared to the analytical solutions of Wannier[47]. Similarly, in Figs. 4 and 5, we plot the streamlines, a color map of the norm of the velocity vector and the azimuthal velocity profile in the large gap region along the $\mathbf{e}_y$ axis. This profile is compared to the theoretical solution by Wannier[47] for all two values of the eccentricity. First, we observe that the numerical and analytical solutions are in very good agreement. We also note that, contrary to a centered Couette flow, a non-zero azimuthal pressure gradient is induced ($\partial p/\partial\theta \neq 0$, Fig. 3). In the main, this pressure gradient is associated with the formation of an additional parabolic (Poiseuille) type flow in the azimuthal direction. The flow may be understood as the superposition of a Poiseuille flow,

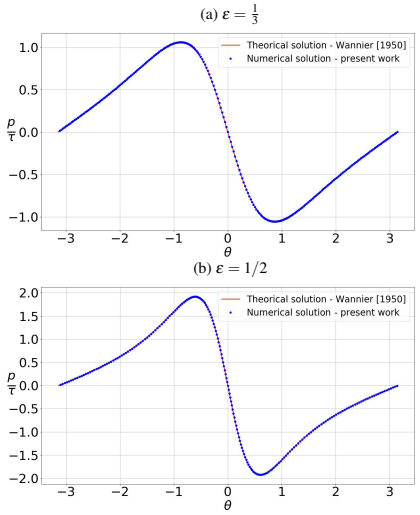

FIG. 3. Pressure profiles at the outer cylinder for eccentricity ratios of: (a) $\varepsilon = \frac{1}{3}$, (b) $\varepsilon = 1/2$. The pressure is normalized by the typical shear stress $\tau = \eta_f \omega R_{in}/(R_{out} - R_{in})$. The red line is the analytical solution of Wannier [47] while the blue points denote the numerical solution of the model used here.

associated with the pressure gradient, and a Couette flow, associated with the rotation of the inner cylinder[60]. Indeed, the flow being incompressible, the flow rate must necessarily be conserved. However, the flow rate of the underlying Couette flow varies with the angular position, since the thickness of the gap varies, while the velocity of the liquid at the inner cylinder does not. Consequently, to ensure this conservation, a Poiseuille flow is generated to counterbalance this flow rate variation. It takes place in the direction of shear, to increase the flow rate, in the narrow region and in the direction opposite to shear, to decrease the flow rate, at the large gap (see Fig. 6). The greater the eccentricity, the stronger the Poiseuille flow. As displayed in Figs. 4 and 5, the azimuthal pressure gradient may considerably alter the flow. While at $\varepsilon = 1/3$, the overall features of a centered Couette flow are recovered, it is not the case for the larger value $\varepsilon = 1/2$, where a recirculation flow takes place in the large gap region. In the latter case, the Poiseuille flow is strong enough to reverse the velocity and to induce this recirculation flow. In Figs. 7a and 8a, we plot the χ classification criterion – Eq. (8) – introduced by Ryssel and Brunn[61]:

$$\chi = \frac{2\|\mathbf{\Delta\Omega}\|}{\frac{\dot{\gamma}}{2} + \|\mathbf{\Delta\Omega}\|} \tag{8}$$

with $\mathbf{\Delta\Omega} = \mathbf{\Omega}_E - \mathbf{\Omega}$, the relative angular velocity of the strain rate tensor with respect to the liquid (see Badia *et al.* [1]). This criterion is used to classify the type of flow : $\chi \to 0$ corresponds to a pure extensional flow, $\chi \to 1$ to a simple shear flow and $\chi \to 2$ to a solid-body rotation. We observe that, for $\varepsilon = 1/3$ (Fig. 7a), the flow is a simple shear flow over the whole domain, while for $\varepsilon = 1/2$ (Fig. 8a), solid-body rotation and pure extensional flow take place over a thin zone within the recirculation area. The position of this latter zone is a bit counterintuitive since it may have been expected that the extensional flow zones would be located near the narrow gap region, where the gap narrows and then widens. It should also be noted that the solid body rotation region is not situated right at the center of the recirculating area, where the shear rate keeps a finite value. Actually, the solid-body rotation and pure extension regions are located in the vicinity of the regions where the shear rate vanishes (Fig. 8b). These regions exist only when a recirculating flow is generated. It should be noted that in the $\varepsilon = 1/3$ case, the shear rate vanishes at the outer cylinder in the large gap region (Fig. 7b), as it vanishes in the solid-body rotation region for the $\varepsilon = 1/2$ case (Fig. 8). The reason is the following: the value $\varepsilon = 1/3$ corresponds (at least approximately) to the particular value of the eccentricity beyond which the recirculation flow occurs. We can therefore observe the beginning of this recirculation in Fig. 7b.

B. Suspension flow

We are interested here in an isodense suspension flow ($\rho_p = \rho_f$) in an eccentric Couette geometry. We take up the experiments by Subia *et al.* [2] whose geometry is the same as in the previous section. The mixture is composed of PMMA particles of radius $a = 337.5\ \mu m$ and density $\rho_p = 1180\ kg.m^{-3}$, suspended in a Newtonian fluid of viscosity $\eta_f = 4.95\ Pa.s$ and density identical to that of the solid. The inner cylinder rotates at an angular velocity of $\omega = 90\ rpm$ corresponding to the Reynolds number $Re = (R_{out} - R_{in})R_{in}\omega\rho_f/\eta_f \approx 0.27$. In the initial state, the Couette contains a uniform suspension of concentration $\phi_{bulk} = 0.5$. In order to better visualize the influence of the eccentricity, we start with the simulation of a centered geometry ($\varepsilon = 0$). The numerical calculations are performed on the same $2D$ mesh as in the previous section (Fig. 2).

It is well known that particles in a Couette flow migrate from the inner cylinder to the outer cylinder, i.e. to the low shear rate region[7,8,10,43]. In the present case (Fig. 9), since the gap ($R_{out} - R_{in}$) is quite large and the initial concentration is high, migration is considerable and the suspension is jammed ($\phi_m = 0.583$) close to the outer cylinder.

The simulations of the experiments by Subia *et al.* [2] for eccentricity ratio of $\varepsilon = 1/3$ and $\varepsilon = 1/2$ yield numerical data in fair agreement with the experimental measurements both in steady flow (Fig. 10) and during the transient migration (Fig. 11). This constitutes an additional validation of the model developed by Badia *et al.* [1]. As shown in Fig. 12, the steady concentration distribution is strongly affected by the eccentricity. Indeed, for the lowest eccentricity ratio $\varepsilon = 1/3$, jamming is reached in the large gap near the outer cylinder, similarly to the case of the centered Couette geometry. In contrast, for an eccentricity ratio of $\varepsilon = 1/2$, jamming does not occur near the outer cylinder but rather within the recirculation zone. Moreover, as experimentally and numeri-

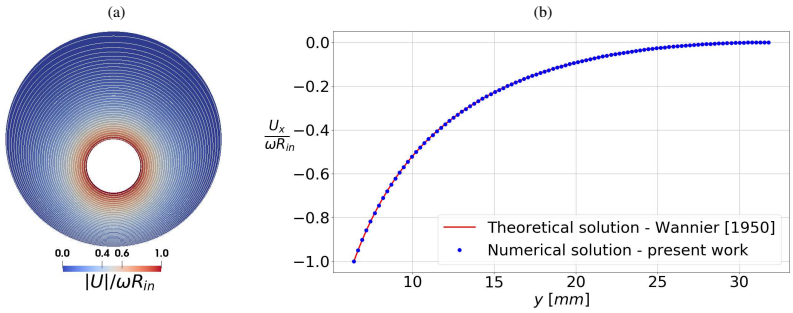

FIG. 4. Flow velocity normalized by the velocity at the inner cylinder ωR_{in} for $\varepsilon = 1/3$: (a) streamlines and velocity norm, (b) azimuthal velocity profile across the large gap along the $\mathbf{e}_y$ axis.

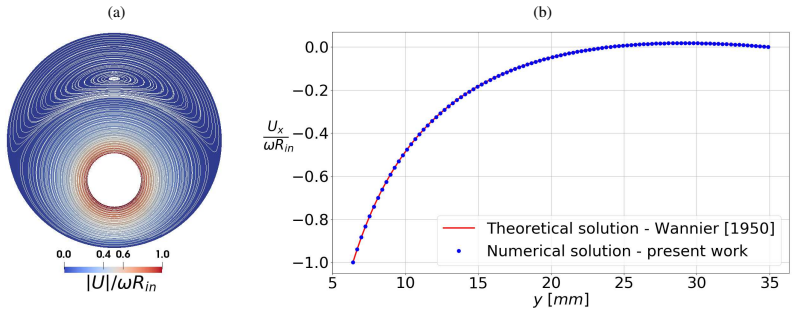

FIG. 5. Flow velocity normalized by the velocity at the inner cylinder ωR_{in} for $\varepsilon = 1/2$: (a) streamlines and velocity vector norm, (b) azimuthal velocity profile across the large gap along the $\mathbf{e}_y$ axis.

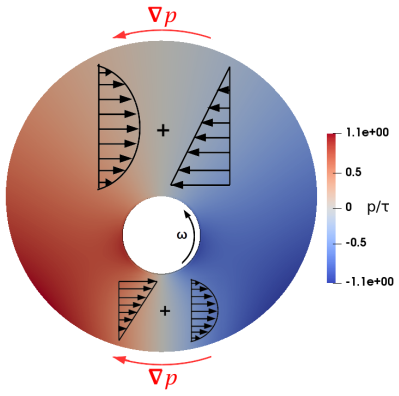

FIG. 6. Numerical pressure distribution, normalized by $\tau = \eta_f \omega R_{in}/(R_{out} - R_{in})$, for $\varepsilon = 1/3$. Illustration of the flow which may be understood as a superposition of Couette flow and Poiseuille flow.

cally observed by Subia *et al.* [2], symmetry breaking occurs for both values of the eccentricity ratio. In both cases, the steady volume fraction and shear rate distributions are tilted toward the counterclockwise direction. In addition, for the largest value of the eccentricity ratio $\varepsilon = 1/2$, a strong modulation of both distributions occurs in the wide gap region, starting from the entrance of the expansion area, due to the recirculation flow, which is rather inclined toward the clockwise direction (Fig. 12c-12d). Figure 12 also shows that the volume fraction distribution has the same general features as the shear rate distribution for both values of the eccentricity ratio. The concentration is higher in low shear rate locations, that is consistent with the usual direction of particle migration: in the $\varepsilon = 1/2$ case, the region of lowest shear rate moves to the center of the recirculation area, while in the $\varepsilon = 1/3$ case, it is found in the vicinity of the outer cylinder. Finally, in both cases, particle migration interacts with the convective transport of particles and contributes to generate a complex asymmetric flow.

When considering the flow kinematics again, it can be observed (Fig. 13) that the χ classification criterion for this suspension flow gives the same result as for a Newtonian fluid in the case of $\varepsilon = 1/3$, i.e. the flow is everywhere a simple shear. In the case of $\varepsilon = 1/2$, the solid–body rotation zone is larger,

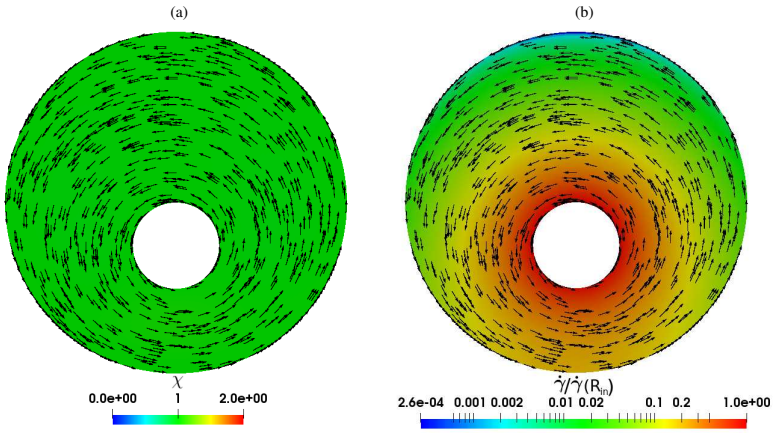

FIG. 7. Representation of the flow kinematics for $\varepsilon = 1/3$: (a) Flow classification with the χ criterion, (b) shear rate $\dot{\gamma}$ normalized by the shear rate near the inner cylinder $\dot{\gamma}(R_{in})$.

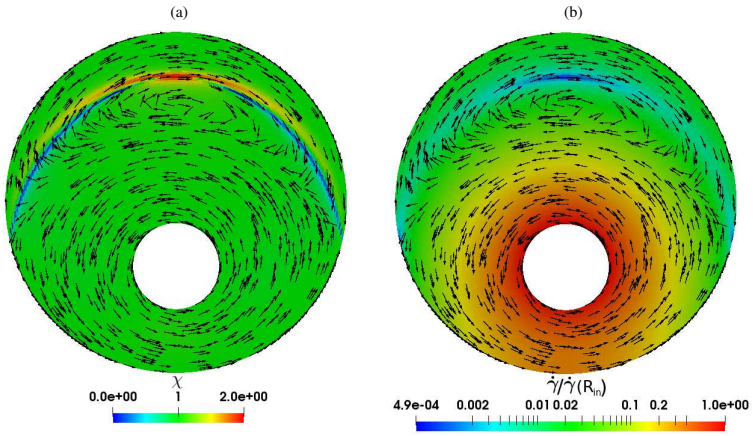

FIG. 8. Representation of the flow kinematics for $\varepsilon = 1/2$: (a) Flow classification by χ criterion, (b) shear rate $\dot{\gamma}$ normalized by the shear rate near the inner cylinder $\dot{\gamma}(R_{in})$.

and not symmetrical with respect to the symmetry axis of the geometrical boundaries which is most probably due to the increase of the concentration in the centre of the recirculation zone.

As a conclusion, as already shown by Subia *et al.* [2], the eccentric Couette flow of non-Brownian suspensions, for sufficiently high eccentricity ratio, presents significant complexity due to the feedback of particle migration on the development of the recirculation flow. This results in particular in an altered shear rate distribution, compared to the Newtonian fluid flow, where the symmetry of the geometrical boundaries is broken. Noticeably, the volume fraction distribution approximately mirrors the shear-rate distribution. The flow complexity is also reflected by the distribution of the reduced angular velocity difference χ, according to which the flow in the recirculation region rather approaches a rigid body motion. The present numerical modelling proves to be able to accurately tackle all aspects of this complex flow, including velocity and volume fraction distributions in transient and steady flow, and their variation with the eccentricity.

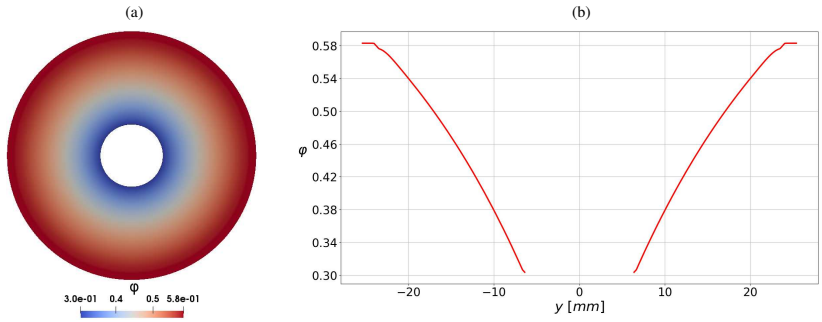

FIG. 9. Computed volume fraction distribution for $\varepsilon = 0$ at steady state: (a) color map over the whole domain (b) radial profile along the $\mathbf{e}_y$ axis.

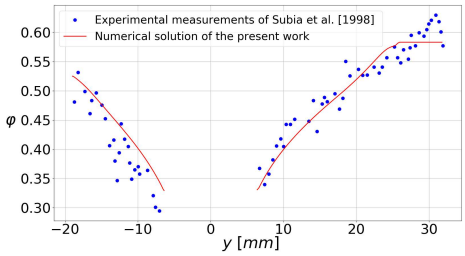

FIG. 10. Volume fraction along the $\mathbf{e}_y$ axis for $\varepsilon = 1/3$ at steady state. The blue points correspond to the experiments by Subia *et al.* [2] while the red line represents the numerical solution of the model used here.

IV. VISCOUS RESUSPENSION

Viscous resuspension refers to the process during which, under the effect of shear, a bed of initially sedimented dense particles becomes suspended. We simulate in the present section a cylindrical Couette cell containing a suspension of initially settled dense particles ($\rho_p > \rho_f$). As the inner cylinder begins to rotate, the contact stresses induce an upward flux of particles, opposing the effect of gravity until a stationary state is reached. The particles are then distributed non-uniformly throughout the Couette flow.

In Section IV A, a centered geometry will be addressed, mostly as a validation of the numerical modelling – Eqs. (1). To this purpose, the data from the numerical computation will be compared to analytical solutions and experimental measurements. In Section IV B, the viscous resuspension in an eccentric cylindrical Couette geometry will be considered, and the influence of the eccentricity established.

A. Centred Cylindrical Couette Geometry

Acrivos, Mauri, and Fan [17] studied the resuspension of different types of mixtures in a small gap cylindrical Couette geometry. With an assumed constant shear rate across the gap, they showed that the reduced resuspension height h/h_0 was function of the Shields number A only. It is defined by :

$$A = \frac{9}{2}\frac{\eta_f \dot{\gamma}}{g\left(\rho_p - \rho_f\right) h_0} \tag{9}$$

with h_0 the initial height of the sediment and g the gravitational acceleration. This parameter represents the ratio between the viscous forces and the apparent weight. Before comparing the numerical results of our model with the experimental results of Acrivos, Mauri, and Fan [17], it is possible to compute a semi-analytical stationary solution for this problem. Indeed, as the gap is small compared to the inner radius, the shear rate is assumed to be constant. The particle volume conservation equation (Eq. (1c)) then becomes in the steady state equivalent to an ODE. In more detail, it is assumed that the suspension velocity is written as $\mathbf{u} = u_\theta(r)\mathbf{e}_\theta$, while the balance equation for the angular momentum yields $\dot{\gamma} = C/r^2\eta_f\eta_s$, where C is a constant[1]. When the gap is narrow, the shear rate is almost constant, and particle migration is weak. It is assumed here that the gap is narrow enough for the radial migration to be neglected. Moreover, the suspension acceleration $\|D\mathbf{u}/Dt\|$ is of the same order of magnitude as $r\omega^2$, and in the present problem we consider angular velocities such that $r\omega^2/g \ll 1$. These assumptions are equivalent to considering a flow between two parallel vertical plates for which the shear rate is uniformly equal to $\omega R_{in}/(R_{out} - R_{in})$. The volume fraction is assumed to depend only on height z. In this case, Eq. (1c) writes at steady state ($\partial\phi/\partial t = 0$) :

$$\frac{d}{dz}\left(-\phi\frac{2a^2 f(\phi)}{9\eta_f}(\rho_p - \rho_f)g + \frac{2a^2 f(\phi)}{9\eta_f} \times \frac{d\,\Sigma^c}{dz}\right) = 0 \tag{10}$$

Hence the sum of the sedimentation and migration fluxes is equal to a constant, which amounts to the total flux at the bot-

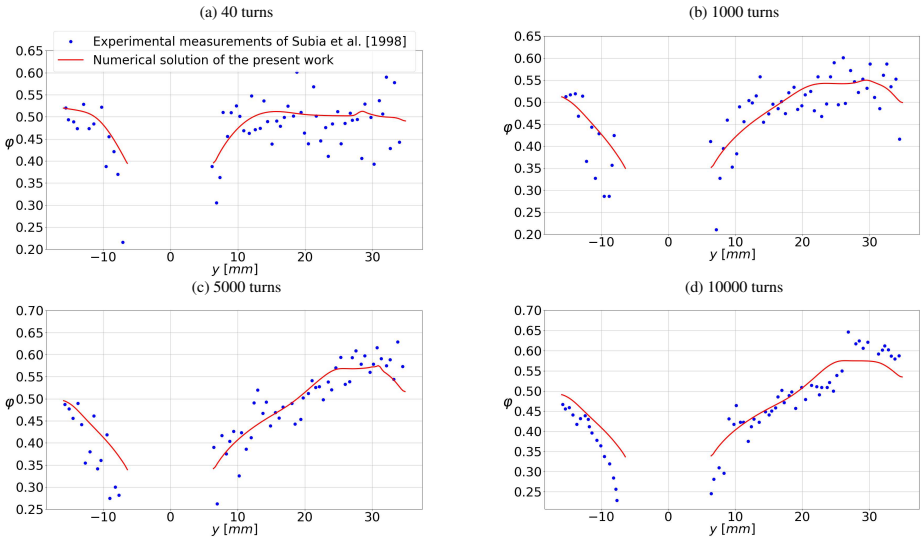

FIG. 11. Volume fraction profile at different times along the $\mathbf{e}_y$ axis for $\varepsilon = 1/2$: (a) 40 turns, (b) 1000 turns, (c) 5000 turns, (d) 10000 turns. The numerical solution corresponds to the red curve while the experimental measurements by Subia *et al.* [2] are represented by blue points.

tom of the Couette cell, i.e. zero :

$$\frac{d\,\Sigma^c_{zz}}{dz} - (\rho_p - \rho_f) g \phi = 0 \tag{11}$$

In our specific flow geometry, Σ^c_{zz} is actually the normal contact stress in the vorticity direction in a simple shear flow $\Sigma^c_{33} = \eta_s(\phi)\hat{\Sigma}^c_{33}(\phi)\eta_f\dot{\gamma}$. Since $\dot{\gamma}$ does not depend on z, the relevant dimensionless ODE – Eq. (12a) – is easily deduced, where A is the Shields number and $\hat{z} = z/h_0$. This ODE is solved with the constraint that the total particle volume is constant, as written in Eq. (12b), where h is the height of the resuspended layer and h_0 is the initial height of the sediment of concentration ϕ_m.

$$\frac{d\phi}{d\hat{z}} - \frac{9}{2}\frac{1}{A\frac{d}{d\phi}\left(\eta_s\hat{\Sigma}^c_{33}\right)}\phi = 0 \tag{12a}$$

$$\int_0^{\frac{h}{h_0}} \phi(\hat{z})\, d\hat{z} = \phi_m \tag{12b}$$

Moreover, it is also possible to demonstrate from the above equations that the resuspension height, h, only depends on the Shields number, as was done by Acrivos, Mauri, and Fan [17]. Indeed, after a change of variable, Eq. (12a) yields the following expressions:

$$\frac{h}{h_0} = -\frac{2}{9}A\int_0^{\phi(0)} \frac{1}{\phi}\frac{d}{d\phi}(\eta_s\hat{\Sigma}^c_{33})\, d\phi \tag{13a}$$

$$\int_0^{\frac{h}{h_0}} \phi d\hat{z} = -\frac{2}{9}A\int_0^{\phi(0)} \frac{d}{d\phi}(\eta_s\hat{\Sigma}^c_{33})\, d\phi \tag{13b}$$

where $\phi(0)$ is the unknown volume fraction at $z = 0$. Combining equations (12b) and (13b), we obtain:

$$-\frac{2}{9}\frac{A}{\phi_m}\int_0^{\phi(0)} \frac{d}{d\phi}(\eta_s\hat{\Sigma}^c_{33})\, d\phi = 1 \tag{14}$$

Thus, Eq. (14) shows that $\phi(0)$ depends only on Shields number A. Finally, by combining equations (13a) and (14), we obtain:

$$\frac{h-h_0}{h_0} = \frac{2}{9}A\int_0^{\phi(0)} \left(\frac{1}{\phi_m} - \frac{1}{\phi}\right)\frac{d}{d\phi}(\eta_s\hat{\Sigma}^c_{33})\, d\phi \tag{15}$$

This clearly shows that for a given ϕ_m, the relative variation of the resuspension height $(h-h_0)/h_0$ only depends on the Shields number A.

The solution of the equations (12) is now to be compared with the volume fraction profile from the numerical simulations. The geometry consists of a narrow gap cylindrical Couette cell with $R_{in}/R_{out} \approx 0.92$ ($R_{out} - R_{in} = 2\ mm$). The suspension is made of particles of radius $a = 69.5\ \mu m$ and density $\rho_p = 2450\ kg/m^3$ in a fluid of viscosity $\eta_f = 0.47\ Pa.s$ and density $\rho_f = 980\ kg/m^3$ $\left(\rho_p/\rho_f = 2.5\right)$. The initial height of the sediment is chosen equal to $h_0 = 9.18\ mm$ $(h_0/a \approx 132)$. The outer cylinder is fixed while the inner cylinder rotates at an angular velocity ω giving the dimensionless parameters: $A = 0.73$, $Re = (R_{out} - R_{in})R_{in}\omega\rho_f/\eta_f = 0.367$ and $\omega^2 R_{in}/g = 0.034$. The mesh of our numerical simulation is $3D$ with 80 grid points in the azimuthal direction and 15 in the radial direction. In order to examine the influence of the grid step size in the vertical direction on the clear fluid/suspension

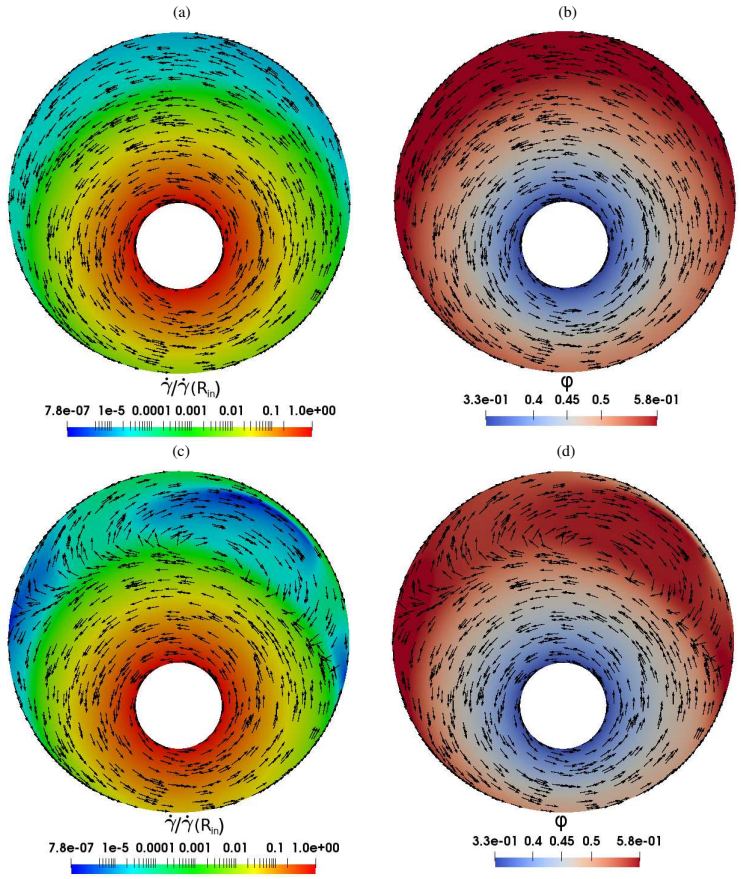

FIG. 12. Shear rate distribution $\dot{\gamma}/\dot{\gamma}(\mathrm{R_{in}})$ (normalized by the shear rate near the inner cylinder) in logarithmic scale and volume fraction φ : (a) and (b) $\varepsilon = 1/3$ at steady state ($\approx$ 6800 turns); (c) and (d) $\varepsilon = 1/2$ at 10000 turns.

interface, we perform two different simulations using vertical space steps of respectively $\Delta z_1 = 0.038 h_0$ and $\Delta z_2 = \Delta z_1/4$.

In Fig. 14, we represent volume fraction profile frome the numerical simulations compared to the ODE solution (12) computed using a multistep backward differentiation formula method from the Scipy library, suitable for stiff equations. The volume fraction is plotted as a function of z at the center of the gap (i.e., for $r = R_c = (R_{out} + R_{in})/2$). We observe a very good agreement except near the clear fluid-suspension interface. Indeed, the theoretical volume fraction presents an infinite derivative at this location. This is explained by the very low values taken by $\eta_S \hat{\Sigma}^c_{33}(\phi)$ – actually its derivative in Eq. (12) – as soon as the volume fraction is lower than about thirty percent[1]. As a consequence, the volume fraction changes very rapidly in an undersampled area, and the numerical solution is therefore strongly influenced by the mesh size. Consistently, dividing the mesh size by 4 reduces the maximum difference between the two numerical curves by approximately the same amount. In addition, we note that the numerical results show a radial variation of the shear rate of $(\dot{\gamma}(R_{in}) - \dot{\gamma}(R_{out}))/\dot{\gamma}(R_c) \approx 0.16$ and a radial change in volume fraction of $(\phi(R_{out}) - \phi(R_{in}))/\phi(R_c) \approx 0.042$, which is, as expected, relatively small. Moreover, the acceleration of the suspension $\|D\mathbf{u}/Dt\|$ obtained numerically is negligible compared to the gravitational acceleration $(\max(\|D\mathbf{u}/Dt\|)/g \approx 0.04 \ll 1)$, and the term $\boldsymbol{\nabla}.(\phi\mathbf{u})$ is very small compared to the other terms of the Eq. (1c). This confirms the assumptions made for the derivation of the semi-analytical solution and validates the numerical solution of this problem.

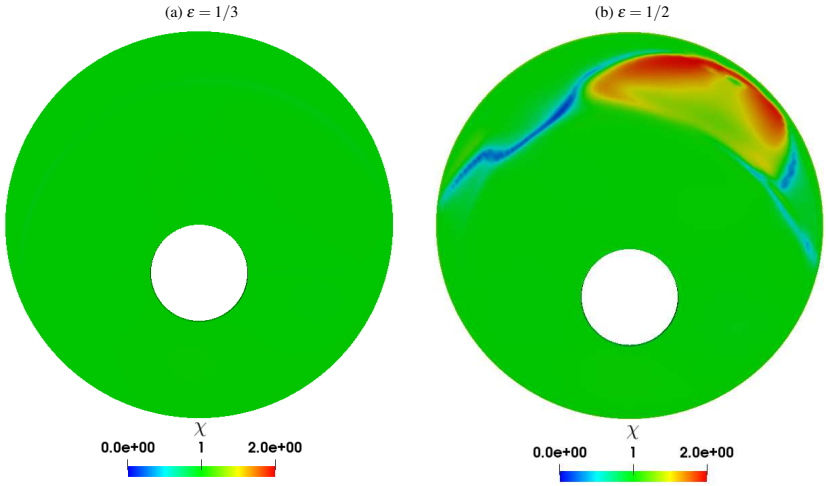

FIG. 13. Classification by the criterion χ of the suspension flow with an initial concentration $\phi_{bulk} = 0.5$: (a) $\varepsilon = 1/3$, (b) $\varepsilon = 1/2$.

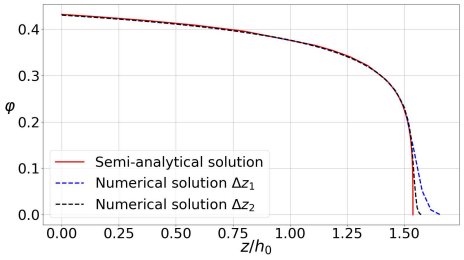

FIG. 14. Vertical volume fraction profile calculated at the center of the gap for $A = 0.73$ and $h_0 = 0.00918\ m$. Comparison between the semi-analytical solution and the numerical solutions with for the latter a vertical step of $\Delta z_1 = 0.038 h_0$ and $\Delta z_2 = \frac{\Delta z_1}{4}$.

The relative resuspension height $(h - h_0)/h_0$ as a function of the parameter A is shown in Fig. 15. We compare the result of the present model (Eq. (15)) with the theoretical result of the diffusive model used by Acrivos, Mauri, and Fan [17], as well as with their experimental measurements. We observe that the resuspension height from the present model is quite close to their theoretical and experimental results.

We now consider another set of experiments by D'Ambrosio, Blanc, and Lemaire [4], which will be of interest in the next section devoted to the influence of the eccentricity of the geometry. The inner and outer radii are respectively $R_{in} = 19\ mm$ and $R_{out} = 24\ mm$ ($R_{in}/R_{out} \approx 0.79$). The mixture is composed of spherical particles of radius $a = 134\ \mu m$ and density $\rho_p = 1190\ kg/m^3$ in a fluid of viscosity $\eta_f = 0.34\ Pa.s$ and density $\rho_f = 1060\ kg/m^3$ ($\rho_p/\rho_f \approx 1.12$). The initial height of the sediment is $h_0 = 21.3mm \approx 159a$. We present here simulations for two angular velocities, respectively $\omega = 20\ rpm$ and $\omega = 0.5\ rpm$, which yield the following scaled parameters: $A \approx$ resp. 0.45 and 0.011; $Re \approx$ resp. 0.62 and 0.015; $\omega^2 R_{in}/g \approx$ resp. $8.5\,10^{-3}$ and $5.3\,10^{-6}$.

The Shields number A is here based on the shear rate $\dot{\gamma}_c = \omega R_{in}/(R_{out} - R_{in})$. Compared to the experiment of Acrivos, Mauri, and Fan [17], the ratio of the gap to the inner radius is less small and notable radial migration is expected to take place. The radial and vertical mesh sizes are here respectively $\Delta r = (R_{out} - R_{in})/20 \approx 0.012 h_0$ and $\Delta z \approx 0.0023 h_0$.

In Fig. 16, the volume fraction profiles from the simulations and from the experiments by D'Ambrosio, Blanc, and Lemaire [4] are displayed, which are quantitatively quite consistent. Nevertheless, the numerical simulation predicts significant radial migration (Fig. 17) equivalent to that of an isodense case, i.e. for $z/h_0 = 0.94$, a variation of $(\phi(R_{out}) - \phi(R_{in}))/\phi(R_c) \approx 0.108$ for $\omega = 0.5\ rpm$ and $(\phi(R_{out}) - \phi(R_{in}))/\phi(R_c) \approx 0.111$ for $\omega = 20\ rpm$ (we recall that R_c is the radius of the gap center). On the contrary, D'Ambrosio, Blanc, and Lemaire [4] observe a very weak radial migration once resuspension is complete. Although they proposed possible reasons for this lack of migration, no definitive explanation has yet been found, and this problem still remains an open question.

In such a resuspension experiment, assuming that the flow is locally a simple shear flow, it is possible to determine the material function, $\hat{\Sigma}^c_{33}$, from the volume fraction profile [3,4,43] using Eq. (11), and identifying Σ^c_{zz} with $\eta_s \hat{\Sigma}^c_{33} \eta_f \dot{\gamma}$. It is instructive here to follow the same approach to compute the vertical profile of Σ^c_{zz} using the volume fraction profile $\phi(z)$

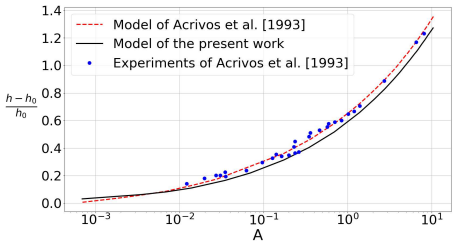

FIG. 15. Relative resuspension height as a function of Shields number A. Red line: theoretical prediction of the model by Acrivos, Mauri, and Fan [17]; Black line: theoretical prediction of the present model; Blue dots: experimental measurements by Acrivos, Mauri, and Fan [17] for 4 different suspensions.

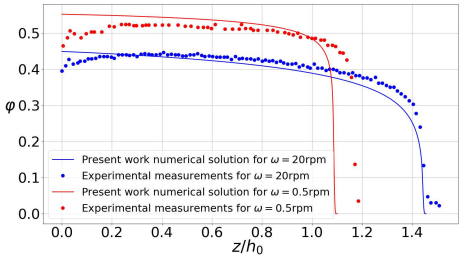

FIG. 16. Vertical concentration profile obtained by averaging $\phi(r)$ over the central third of the gap. Comparison between the present numerical simulation and the experiments by D'Ambrosio, Blanc, and Lemaire [4] for $\omega = 20\ rpm$ and $\omega = 0.5\ rpm$.

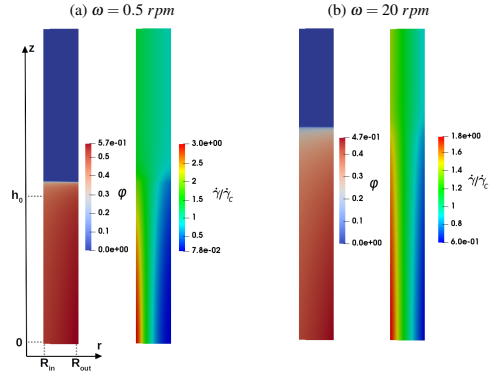

FIG. 17. Steady state color map of shear rate (normalized by $\dot{\gamma}_c = \omega R_{in}/(R_{out} - R_{in})$) and volume fraction for: (a) $\omega = 0.5\ rpm$ and (b) $\omega = 20\ rpm$.

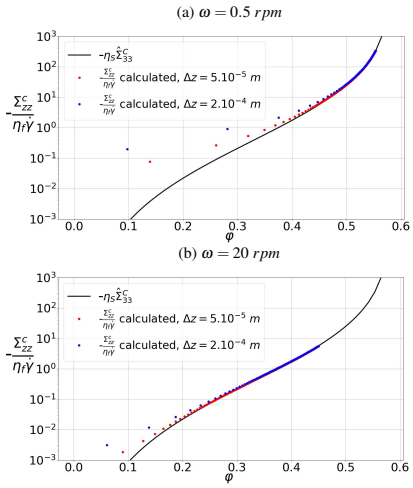

FIG. 18. Normalized contact stress in the vorticity direction for two values of the angular velocity: (a) $\omega = 0.5\ rpm$, (b) $\omega = 20\ rpm$. The black curve represents the expression of $-\eta_s\hat{\Sigma}^c_{33}$, the symbols represent the stress calculated from Eq. (11) with $\Delta z = 9.39 \times 10^{-3}\ h_0$ (blue bullets) and the red dots the stress calculated with $\Delta z = 2.35 \times 10^{-3}\ h_0$ (red bullets).

from the numerical data. This "experimental" determination of $\Sigma^c_{zz}(\phi)$ may then be compared to the shear flow constitutive law $\eta_s\hat{\Sigma}^c_{33}\eta_f\dot{\gamma}$ that was inserted in Eq. (11) (and in the suspension modelling in the simulations Eq. (4b)), allowing to validate such an experimental procedure. Figure 18 presents the variation of $\eta_s\hat{\Sigma}^c_{33}$ (see[1]) compared to the values of $\Sigma^c_{zz}/\eta_f\dot{\gamma}$ calculated from the numerical data in Fig. 16 using Eq. (11). This comparison is performed for the angular velocities $\omega = 20\ rpm$, $\omega = 0.5\ rpm$ and for two different mesh sizes $\Delta z = 2.35 \times 10^{-3}\ h_0$, $\Delta z = 9.39 \times 10^{-3}\ h_0$. We observe a very good agreement, except at low concentration, where the calculated stress deviates from the value of the corresponding material function. This discrepancy is actually due to the finite spatial sampling of the computation volume, which, as previously mentioned, induces numerical errors in the region close to the suspension surface. In this location, according to Eq. (12a), the derivative $d\phi/dz(z = h)$ is theoretically infinite in absence of radial migration, since $\Sigma^c_{zz} \sim \phi^4$ at low volume fraction[1]. As an illustration, decreasing the mesh size narrows the volume fraction range where discrepancy occurs. As observed in Fig. 18, dividing the mesh size by 4 results in the decrease of the volume fraction value below which an error of 10% is observed : at $\omega = 20\ rpm$, this volume fraction cut off decreases from 0.32 to 0.22, and from 0.50 to 0.44 at $0.5\ rpm$. In the same line, a lower angular velocity results in weaker resuspension, meaning in particular that the stiff region of the volume fraction profile extends over a wider volume fraction range, and the volume fraction cut-off is increased (Fig. 18).

B. Eccentric cylindrical Couette geometry

We now consider particle resuspension in an eccentric cylindrical Couette geometry. In this section, we will expose an effect observed in experiments and still not clearly understood. In some resuspension experiments, it can be observed that the surface of the resuspended material is not horizontal, i.e. the resuspension height near the inner cylinder is different from that near the outer cylinder. In addition, the height varies in the azimuthal direction as well as in the radial direction. As shown in the following, this behaviour is in fact caused by a slight eccentricity of the Couette flow geometry. In addition, even a very small eccentricity yields significant variation in the height of the sediment.

This study has been triggered by preliminary experiments conducted by D'Ambrosio, Blanc, and Lemaire[4]. The authors carried out resuspension experiments whose first (unpublished) measurements showed a sediment surface tilted from the horizontal (see Fig. 19b). Independently, Saint-Michel *et al.*[3] published the results of their own resuspension experiments, where a slight variation in sediment height in the gap was also observed. In addition, Saint-Michel *et al.*[3] had access to two diametrically opposite vertical sections. They observed that the sediment heights were different in these two sections. Considering these observations, we simulated the experiments performed in both aforementioned papers by inserting a slight offset between the location of the axes of the inner and outer cylinders. As shown in the following, we were able to establish that this offset was the actual cause of the variations of the sediment height with the position in the gap. For example, this offset has been estimated in the case of the experiments shown in Fig. 19b to 250 μm, which is smaller than the diameter of a particle. Knowing that the gap thickness is 5 mm, it amounts to an eccentricity of 5%. Thus, a small eccentricity leads to a non negligible variation of the resuspension height. We present in the following a numerical study of this behaviour.

It should be stressed that the flow that is presently tackled is quite complex, and in particular, 8 dimensionless numbers, among which 7 are independent, are necessary to conveniently define the flow (Appendix A). The general study of the influence of each dimensionless number is out of the scope of the present paper, which will focus instead on the mentioned two recent experiments.

Geometry of the experiments by D'Ambrosio, Blanc, and Lemaire[4]

We first consider the preliminary experiments carried out by D'Ambrosio, Blanc, and Lemaire[4], whose parameters are described in section IV A. The $3D$ geometry is discretized into 80 mesh cells in the azimuthal direction, 15 cells in the radial direction, and 150 cells in the vertical direction. We present in Fig. 19 a vertical section of the Couette geometry ($\varepsilon = 0.05$) for two values of the angular velocity. The radial variation in sediment height from the simulation is qualitatively the same as from the experiments.

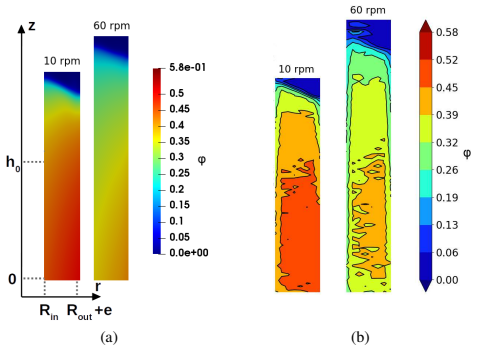

FIG. 19. Color map of the volume fraction $\phi(r,z)$ on a vertical section of the eccentric Couette cell ($\varepsilon = 0.05$) for angular velocities of $\omega = 10\ rpm$ and $\omega = 60\ rpm$: a) simulations using the present model, b) preliminary experiments by D'Ambrosio, Blanc, and Lemaire[4].

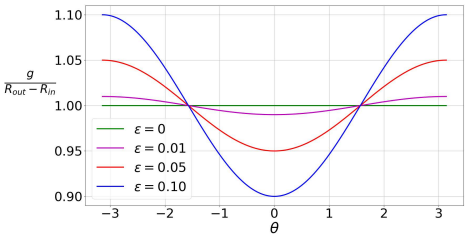

FIG. 20. Variation of the gap $g(\theta)$, normalized by $R_{out} - R_{in}$, as a function of θ. Geometrical parameters from[4].

To accurately determine the influence of the eccentricity, we fix the angular velocity of the inner cylinder at $\omega = 60$ rpm and extend the simulation to eccentricity ratios of $\varepsilon = 0$, $\varepsilon = 0.01$, $\varepsilon = 0.05$ and $\varepsilon = 0.1$. Since the Couette cell is eccentric, the thickness of the gap is no longer uniform and varies with angle θ. Considering that the cylinders radii are quite close to each other, an expression for the approximate value of the thickness, denoted by $g(\theta)$, can be written as :

$$g(\theta) \approx (R_{out} - R_{in})(1 - \varepsilon\cos(\theta)) \tag{16}$$

The function $g(\theta)$ is represented in Fig. 20.

Figure 21 displays a vertical cross–section of the concentration at $\theta = 0$ (narrowest gap) and $\theta = \pi$ (widest gap) for the different values of the eccentricity. We observe a variation of the sediment height across the gap, which is more pronounced as the eccentricity increases. Moreover, for largest values of the eccentricity (Fig. 21c and Fig. 21d), the average resuspension height across the gap is larger at $\theta = 0$, where the gap is smaller, and the asymmetry is stronger in these two cases. To be more specific, the variation of $\hat{h}$, the resuspension height normalized by its counterpart in the centered case, is shown in Fig. 22. We observe that eccentricity increases the average resuspension height, both at the inner and outer cylindrical wall

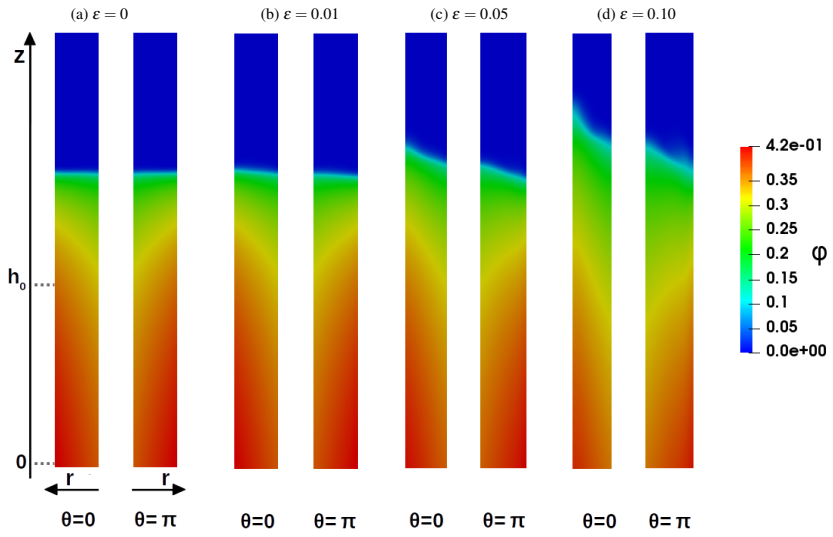

FIG. 21. Vertical cross-section of the concentration at $\theta = 0$ (narrower gap) and $\theta = \pi$ (wider gap) for angular velocity $\omega = 60\ rpm$ and for different values of the eccentricity ratio: (a) $\varepsilon = 0$, (b) $\varepsilon = 0.01$, (c) $\varepsilon = 0.05$, (d) $\varepsilon = 0.1$.

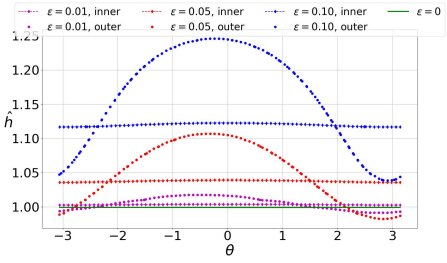

FIG. 22. Resuspension height, normalized by the height of the centered case, as a function of θ near the outer and inner cylinders and for different values of the eccentricity ratio. Geometrical parameters from[4].

(Table I). Moreover, while the normalized height $\hat{h}$ weakly changes with the angle θ near the inner cylinder, it varies considerably near the outer cylinder, and this all the more as the eccentricity increases. The slope of the resuspended layer surface, $(h_{out} - h_{in})/(R_{out} - R_{in})$, also depends on θ, and the amplitude of its variation in the azimuthal direction increases with the eccentricity. Finally, the maximum value of the reduced height at the outer cylinder is found closer and closer to $\theta = 0$ as the eccentricity increases.

Inspection of the pressure variations is also instructive. To this purpose, the pressure and the azimuthal pressure gradient at the height of $20mm \approx h_0$ at the inner and outer cylinders are displayed in Fig. 23. As explained in the previous sections, the eccentricity induces an azimuthal pressure gradient,

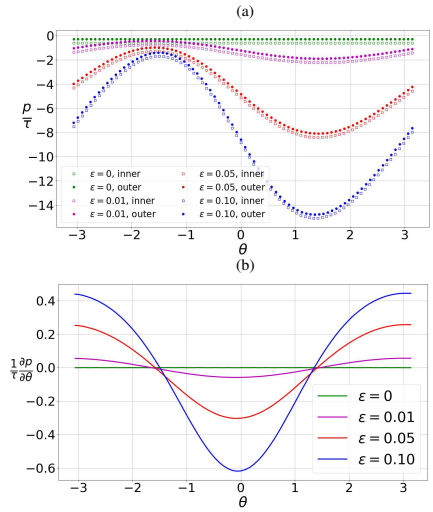

FIG. 23. (a) Pressure, normalized by typical shear stress $\tau = \eta_f \omega R_{in}/(R_{out} - R_{in})$, as a function of θ at the inner and outer cylinders and for different values of the eccentricity ratio. The pressure is measured at the height of 20 mm for angular velocity $\omega = 60\ rpm$. (b) Azimuthal pressure gradient as a function of θ and for different values of the eccentricity ratio. Geometrical parameters from[4].

TABLE I. Simulation results for the geometry of[4]: for each eccentricity ratio ε, are presented, respectively, the normalized height mean value at the inner and outer cylinders, the amplitude of variation with the angle normalized by the mean value at the inner and outer cylinders, and finally the maximum and minimum slope of the resuspended layer surface.

ε	$\bar{\hat{h}}_{in}$	$\bar{\hat{h}}_{out}$	$\frac{\hat{h}_{in}^{max}-\hat{h}_{in}^{min}}{\bar{\hat{h}}_{in}}$	$\frac{\hat{h}_{out}^{max}-\hat{h}_{out}^{min}}{\bar{\hat{h}}_{out}}$	$\max\left(\frac{h_{out}-h_{in}}{R_{out}-R_{in}}\right)$	$\min\left(\frac{h_{out}-h_{in}}{R_{out}-R_{in}}\right)$
0.01	1.0033	1.005	0.001	0.026	0.094	-0.077
0.05	1.038	1.048	0.003	0.119	0.47	-0.367
0.10	1.120	1.155	0.005	0.180	0.846	-0.537

and the higher the eccentricity, the stronger the pressure gradient (the pressure difference between inner and outer bounding cylinders originates in the inertia of the suspension). Moreover, according to Figs. 20 and 23b, the values of θ that define the extremums of the azimuthal pressure gradient (Fig. 23b) approximately correspond to those that define the extremums of the gap thickness, i.e. $\theta = 0$ and $\theta = \pi$ (Fig. 20). All this is qualitatively similar to the $2D$ flow of a Newtonian liquid studied in Section III A. However, in addition to being accelerated or decelerated in the horizontal plane, the fluid here is driven upward or downward.

Geometry of the experiments by Saint-Michel et al. [3]

We now focus on the resuspension experiments by Saint-Michel *et al.* [3], using the same geometry as previously, with an inner radius of $R_{in} = 23$ *mm*, an outer radius of $R_{out} = 25$ *mm*, and a height $H = 53.5$ *mm*. The mixture is composed of particles of density $\rho_p = 2500\ kg.m^{-3}$ and radius $a = 125$ μm, suspended in a fluid of density $\rho_f = 1030\ kg.m^{-3}$ and viscosity $\eta_f = 0.23$ *Pa.s*. The initial height of the sediment is $h_0 = 70.4a = 8.8$ *mm*. Compared to the geometry in the paper by D'Ambrosio, Blanc, and Lemaire [4], the ratio $(R_{out} - R_{in})/R_{in}$ is significantly smaller, meaning in particular that the shear rate is expected to be more uniform across the gap. As mentioned above, Saint-Michel *et al.* [3] observe a slight slope of the suspension surface and difference in the resuspension height between two opposite sections (ranging from 1% to 9% depending on the shear rate applied). They assume that this is due to a slight misalignment of the geometry since they measure a 3% difference in size between the two sections studied. We simulate this resuspension experiment by applying eccentricity for different shear rate values. Since we ignore the exact value of the eccentricity, we choose $\varepsilon = 0.05$. Simulations are performed for the shear rate values $\dot{\gamma} = \omega R_{in}/(R_{out} - R_{in}) = 25\ s^{-1}$, $50\ s^{-1}$, $100\ s^{-1}$ and $250\ s^{-1}$. The mesh is similar to that in the previous simulation, except that the vertical spatial step has been decreased to $\Delta z = 1.68\ 10^{-3}\ H$.

The resuspension height at the inner and outer cylinders, normalized by its counterpart in the centered geometry, is plotted in Fig. 24 as a function of θ for the different values of the shear rates. As in the previous set of experiments, the mean resuspension height at the inner cylinder is larger than in the centered geometry, and the amplitude of the variation of $\hat{h}$ with the angle is quite low (Table II). In addition, the shear rate hardly changes this amplitude. At the outer cylinder, the amplitude is larger, and the effect of the shear rate on both the mean reduced height and the amplitude is significant. As a consequence, the amplitude of the slope of the resuspended layer in the radial direction increases with the shear rate.

We can also observe qualitative differences between the data from the two simulated geometries (Fig. 22 and 24). Indeed, the maximum of $\hat{h}$ in Fig. 22 is not reached at the same angle as in Fig. 24. This could be explained by the fact that the geometry of Saint-Michel *et al.* [3] has a smaller gap, the radial shear rate weakly varies and therefore the radial migration is negligible, on the contrary to the experiment of D'Ambrosio, Blanc, and Lemaire [4] where the gap is not small and therefore significant particle migration occurs.

In Fig. 25, we plot the resuspension height h at the center of the gap normalized by the initial sediment height h_0 as a function of the Shields number $Sh = \eta_0\dot{\gamma}/(\rho_p - \rho_f)ga$ for the experiments by Saint-Michel *et al.* [3] as well as for the simulation data. This Shields number, used by Saint-Michel *et al.* [3] and based on the size of the particles, is quite similar to A (Eq. (9)), which is based on the suspension depth h_0 though. As to the experimental data, the resuspension height is shown for two diametrically opposite sections of the Couette cell. Concerning the simulation data, since we ignore the position of the sections relative to the narrow section, i.e. the θ angle, where Saint-Michel *et al.* [3] measured the resuspension height, we chose to plot the smallest and largest height measured over one revolution. The experimental and simulation data are in good agreement. An apparent discrepancy is that the curves from the opposite sections in the experiments by Saint-Michel *et al.* [3] are close (0.5% difference for the smallest number of Shields and 10% difference for the largest one) while those from our simulations are further away (16% difference for the smallest number of Shields and 15% difference for the largest one). However, it should be noted that Saint-Michel *et al.* [3] use a different h_0 for each section, i.e. there is a relative difference of 6% between the values of h_0 in the left and the right section. Thus, if the original normalization is applied, the difference between the values of the normalized height in the opposite sections is expected to be larger and qualitatively similar to the simulation data in Fig. 25. But again, it is difficult to compare quantitatively experiments and simulations since we ignore the exact eccentricity in the experimental case.

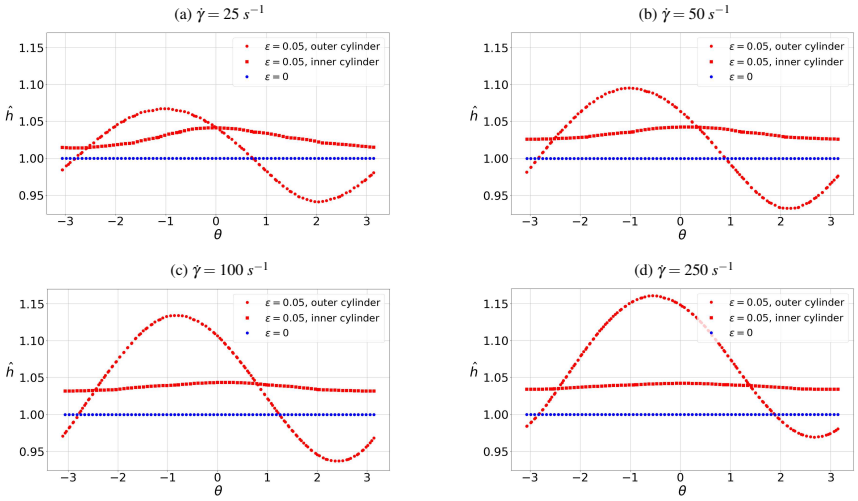

FIG. 24. Resuspension height normalized by the centered case height as a function of θ near the outer and inner cylinders and for different shear rates: (a) $\dot{\gamma} = 25\ s^{-1}$, (b) $\dot{\gamma} = 50\ s^{-1}$, (c) $\dot{\gamma} = 100\ s^{-1}$ and (d) $\dot{\gamma} = 250\ s^{-1}$. The eccentricity ratio is $\varepsilon = 0.05$. Geometrical parameters from[3].

TABLE II. Simulation results for the geometry of Saint-Michel *et al.* [3]: for each shear rate $\dot{\gamma}$, are presented, respectively, the normalized height mean value at the inner and outer cylinders, the amplitude of variation with the angle normalized by the mean value at the inner and outer cylinders, and finally the maximum and minimum slope of the resuspended layer surface.

$\dot{\gamma}\ (s^{-1})$	$\overline{\hat{h}}_{in}$	$\overline{\hat{h}}_{out}$	$\frac{\hat{h}_{in}^{max} - \hat{h}_{in}^{min}}{\overline{\hat{h}}_{in}}$	$\frac{\hat{h}_{out}^{max} - \hat{h}_{out}^{min}}{\overline{\hat{h}}_{out}}$	$\max\left(\frac{h_{out}-h_{in}}{R_{out}-R_{in}}\right)$	$\min\left(\frac{h_{out}-h_{in}}{R_{out}-R_{in}}\right)$
25	1.027	1.008	0.027	0.125	0.230	-0.505
50	1.034	1.016	0.016	0.160	0.392	-0.632
100	1.037	1.036	0.011	0.190	0.670	-0.682
250	1.038	1.066	0.008	0.179	0.951	-0.521

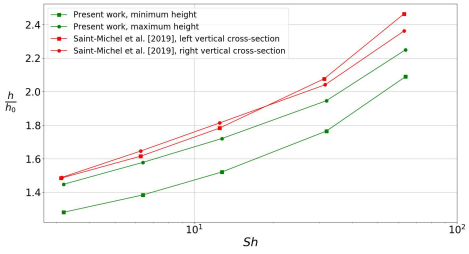

FIG. 25. Resuspension height h calculated at the center of the gap and normalized by the initial sediment height h_0 as a function of the Shields number $Sh = \eta_0\dot{\gamma}/(\rho_p - \rho_f)ga$. The red curves correspond to the experimental results of Saint-Michel *et al.* [3] (right section: circles, left section: squares). The green curves represent the results of the present work for $\varepsilon = 0.05$ (maximum height: circles, minimum height: squares).

Determination of the contact normal stress Σ_{zz}^c

We are now interested in the influence of eccentricity on the calculation of the normal stress in the vorticity direction from the volume fraction vertical profile using Eq. (11), as discussed in Section IV A, in the same geometry as in the experiments by Saint-Michel *et al.* [3]. We first calculate the stress Σ_{zz}^c by integrating the vertical volume fraction profile from the simulation for the centered Couette geometry and compare it to the expression expected in a simple shear flow from the constitutive law that we use , i.e. $\eta_f\eta_s\hat{\dot{\gamma}}\hat{\Sigma}_{33}^c$ – Eq. (4).b. This stress is here normalized by the local shear rate. Again, we observe (Fig. 26) that the "experimental" determination of the stress yields the expected material function, except for the lowest concentrations. However, as shown in Section IV A, the discrepancy is due to the steepness of the $\phi(z)$ profile which induces numerical error in the solution for a given finite mesh size. We now consider the computed stress for the eccentric Couette cell in the center of the gap, i.e. on the cylindrical sur-

face with center O_i and radius $(R_{out}+R_{in})/2$. We observe in Fig. 27 that the stress $\Sigma^c_{zz}/\eta_f\dot{\gamma}$ calculated using Eq. (11) does not correspond exactly to the expression of $\eta_s\hat{\Sigma}^c_{33}$ at low volume fraction. It seems clear that the size of the mesh does not play a decisive role, at least to a first approximation, since the curve resulting from the integration of Eq. (11) separates from the expected curve at a volume fraction that does not depend on the angular velocity, i.e., on the resuspension intensity, as was the case for the centered geometry. Thus Eq. (11) seems not completely valid when the rotor is eccentric. We note that the apparent normal stress is higher than expected, meaning that resuspension is stronger, in agreement with the overall larger observed resuspension height compared to the centered geometry. The explanation may be found in the emergence of fluxes in the vertical and azimuthal directions (see Eq. (1c)) that Eq. (11) does not take into account. To illustrate this idea, the respective divergences of the migration flux $\boldsymbol{\nabla}.\mathbf{J}_{migr}$, of the sedimentation flux $\boldsymbol{\nabla}.(\phi\mathbf{u}_{sed})$ and of the convection flux $\boldsymbol{\nabla}.(\phi\mathbf{u})$ are displayed in Fig. 28 for the centered and eccentric Couette flows. In the case of the centered geometry, the convection contribution is low compared to the other ones, meaning that the net migration flux is balanced by the net sedimentation flux, in agreement with Eq. (11). On the other hand, in the case of the eccentric geometry, the net convection flux contribution is comparable to the other fluxes, and omitting it seems to induce significant imbalance in Eq. (1c). It should be noted that the omitted convection flux shows significant contribution only in the vicinity of the resuspension layer surface, i.e. in the region where the volume fraction is low. As a consequence, the discrepancy between the measured and expected values is only significant at low volume fraction (Fig. 27), where the contact stress is nevertheless very low, which lessens the consequences of such an error in practical situations.

We thus see, in the frame of the present model, the influence that a small eccentricity can have on the measurement of the Σ^c_{zz} stress. However, it should be recalled that we do not take into account here the rheo–fluidification although it seems to play an important role in the experiments[3]. Furthermore, let us recall here that we have chosen contact stress as the driving force for migration. Even though recent particle scale simulations seem to confirm this choice[62], this particular issue is still open, as discussed by Lhuillier[23] and Nott, Guazzelli, and Pouliquen[24], and other choices are conceivable, especially at low volume fraction. It is possible that in this case the eccentricity does not have the same consequences on the measurement of the relevant normal stress, at least quantitatively.

V. CONCLUSION

In this paper, we have presented a numerical study of non-Brownian suspensions in eccentric cylindrical Couette flow, where the axes of the inner and outer cylindrical walls are parallel but not coincident. Both neutrally buoyant and dense suspensions were considered. To this purpose, a recently proposed and validated suspension modelling was used[1]. In the first part, the 2D flow of isodense suspensions was tackled. As an introduction, the standard flow of a Newtonian liquid was considered, allowing to recall the main features of such a flow. The eccentricity creates an azimuthal pressure gradient which generates a Poiseuille flow in addition of the base Couette flow. For a sufficiently large eccentricity, the generated Poiseuille flow is strong enough to locally reverse the velocity and induce a recirculation flow. Moreover, using a kinematic criterion proposed by Ryssel and Brunn[61], it was shown that this flow is purely a simple shear flow at low eccentricity, while purely extensional flow as well as solid body rotation take place in the recirculation region, although over moderate spatial extension.

In the second part of the 2D study, we focused on an isodense suspension, based on the experiments of Subia *et al.*[2]. We observed that migration is influenced by eccentricity, especially when recirculation occurs. The shear rate spatial distribution is indeed different compared to the case of a centred geometry, which affects the volume fraction distribution. The symmetry is broken and, when recirculation takes place, the volume fraction reaches, in the large gap, its maximum value within this recirculation zone, and not at the outer cylindrical wall as evidenced in a centered geometry. Moreover, the comparison of the present simulation data obtained using the suspension modelling developed by Badia *et al.*[1], with the experimental measurements of Subia *et al.*[2] shows fair agreement.

Finally, a 3D study of viscous resuspension in a Couette geometry was conducted, allowing to understand the non-horizontal sediment surfaces observed in some resuspension experiments. First, a study in a centred geometry was performed to evaluate the ability of the suspension modelling and its implementation to handle this type of flow. Then, the study of an eccentric Couette permitted to demonstrate that the eccentricity causes variations of the resuspension height in the radial and azimuthal directions. It also increases the average resuspension height compared to a centred geometry. The numerical computations are in qualitative agreement with the experiments. Finally, we have established that the equation used in experiments to compute the particle normal stress in the vorticity direction from the measurement of the vertical volume fraction profile, may yield somewhat inaccurate results in the eccentric case at low volume fraction due to significant convective flux. In that particular case, the complete particle volume conservation equation should be considered instead of the approximated 1D equation.

More generally, as mentioned at the beginning of Section IV, the eccentric Couette flow of non-Brownian suspensions is controlled by 8 dimensionless numbers, so that it is expected to constitute a complicated issue. The present study is rather descriptive, and is based on the parameters of recent experiments of D'Ambrosio, Blanc, and Lemaire[4] and Saint-Michel *et al.*[3]. This first study may then be complemented by a more comprehensive work in the future.

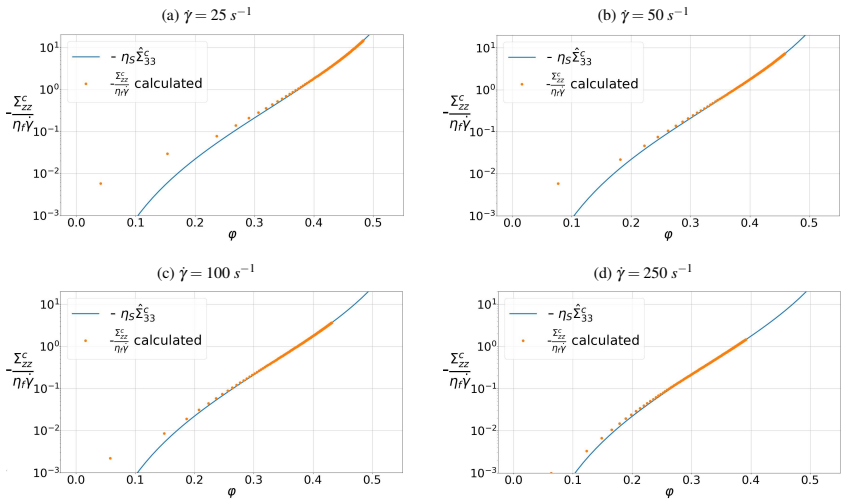

FIG. 26. Normalized contact stress in the vorticity direction for the centered Couette: (a) $\dot{\gamma} = 25\ s^{-1}$, (b) $\dot{\gamma} = 50\ s^{-1}$, (c) $\dot{\gamma} = 100\ s^{-1}$ and (d) $\dot{\gamma} = 250\ s^{-1}$. The blue curve represents the expression of $-\eta_s\hat{\Sigma}^c_{33}$[1], while the orange points correspond to the stress calculated by integrating the vertical volume fraction profile (Eq. (11)). The calculation is performed at the center of the gap, i.e. on the cylinder of center O_i and radius $(R_{out} + R_{in})/2$.

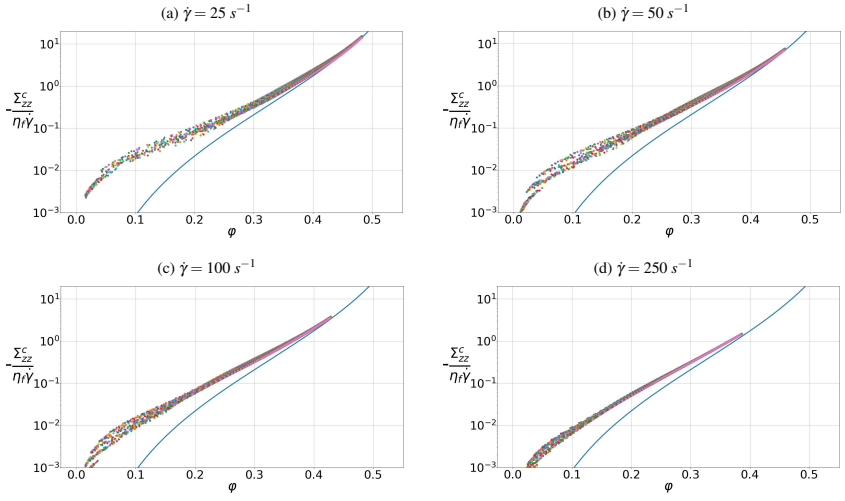

FIG. 27. Normalized contact stress in the vorticity direction for the eccentric Couette ($\varepsilon = 0.05$): (a) $\dot{\gamma} = 25\ s^{-1}$, (b) $\dot{\gamma} = 50\ s^{-1}$, (c) $\dot{\gamma} = 100\ s^{-1}$ and (d) $\dot{\gamma} = 250\ s^{-1}$. The blue curve represents the expression of $-\eta_s\hat{\Sigma}^c_{33}$[1], while the points correspond to the stress calculated by integrating the vertical volume fraction profile (Eq. (11)). The calculation is performed at the center of the gap, i.e. on the cylinder of center O_i and radius $(R_{out} + R_{in})/2$. The different colors of the points correspond to different values of the θ angle.

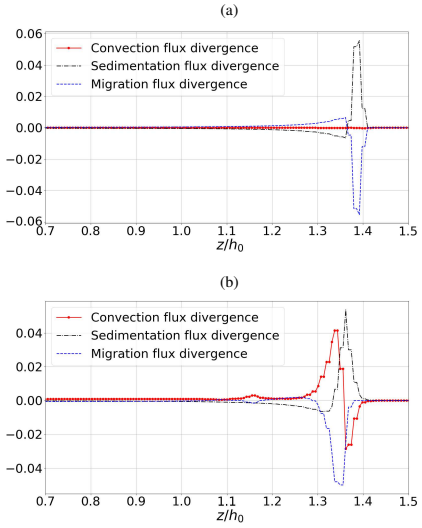

FIG. 28. Vertical profile of the divergence of migration flux, sedimentation flux and convection flux for a centered (a) and eccentric (b) Couette. This profile is determined for the shear rate $\dot{\gamma} = 25\ s^{-1}$.

ACKNOWLEDGMENTS

The authors are pleased to acknowledge Elisabeth Lemaire and Frédéric Blanc for fruitful discussions.

This work was supported by the French government, through the UCAJEDI Investments in the Future project managed by the National Research Agency (ANR) under reference number ANR-15-IDEX-01. The authors are grateful to the OPAL infrastructure from Université Côte d'Azur and the Université Côte d'Azur's Center for High-Performance Computing for providing resources and support.

Appendix A: Dimensionless equations

The purpose of the present section is to exhibit the relevant dimensionless numbers that are sufficient to properly define the excentric Couette flow. For the sake of simplicity, we first make the equations dimensionless, in the simpler case where only one typical length is involved. Let us denote by U and L the relevant velocity and length of the flow. The dimensionless variables are defined as follows:

$$\tilde{\mathbf{u}} = \frac{\mathbf{u}}{U}; \quad \tilde{t} = \frac{tU}{L} = t\dot{\gamma}_c; \quad \tilde{\boldsymbol{\nabla}} = L\boldsymbol{\nabla}; \quad \tilde{a} = \frac{a}{L}$$
$$\tilde{\rho}_m = \frac{\rho_m}{\rho_f}; \quad \tilde{p} = \frac{pL}{\eta_f U} = \frac{p}{\eta_f \dot{\gamma}_c}; \quad \tilde{\dot{\gamma}} = \frac{\dot{\gamma}L}{U} = \frac{\dot{\gamma}}{\dot{\gamma}_c}; \quad \tilde{g} = \frac{gL}{U^2}$$

where $\dot{\gamma}_c = U/L$. Eqs. (1)-(3) write:

$$\tilde{\boldsymbol{\nabla}}.\tilde{\mathbf{u}} = 0 \tag{A1a}$$

$$Re\left(\frac{\partial \tilde{\rho}_m \tilde{\mathbf{u}}}{\partial \tilde{t}} + \tilde{\boldsymbol{\nabla}}.(\tilde{\rho}_m \tilde{\mathbf{u}} \otimes \tilde{\mathbf{u}})\right) - \tilde{\boldsymbol{\nabla}}.\left(\eta_s\left(\tilde{\boldsymbol{\nabla}}\tilde{\mathbf{u}} + \tilde{\boldsymbol{\nabla}}\tilde{\mathbf{u}}^T\right)\right) = -\tilde{\boldsymbol{\nabla}}\tilde{p} + Re\ \tilde{\rho}_m \tilde{\mathbf{g}} + \tilde{\boldsymbol{\nabla}}.(\eta_s \tilde{\dot{\gamma}} \hat{\boldsymbol{\Sigma}}) \tag{A1b}$$

$$\frac{\partial \phi}{\partial \tilde{t}} + \tilde{\boldsymbol{\nabla}}.(\phi \tilde{\mathbf{u}}) + \frac{1}{A}\tilde{\boldsymbol{\nabla}}.\left(\tilde{a}^2 \phi f(\phi) \times \left[\frac{\mathbf{g}}{\|\mathbf{g}\|} - \frac{\frac{D\tilde{\mathbf{u}}}{D\tilde{t}}}{\tilde{g}}\right]\right) = -\tilde{\boldsymbol{\nabla}}.\left(\frac{2\tilde{a}^2 f(\phi)}{9} \times \tilde{\boldsymbol{\nabla}}.\left(\eta_s \tilde{\dot{\gamma}} \hat{\boldsymbol{\Sigma}}^c\right)\right) \tag{A1c}$$

where $\tilde{\rho}_m = (1-\phi) + \phi\rho_p/\rho_f$ and $\hat{\boldsymbol{\Sigma}} = \boldsymbol{\Sigma}/\eta_S \eta_f \dot{\gamma}_c$.

As a consequence, there are 5 dimensionless numbers: the Reynolds number $Re = \rho_f UL/\eta_f$, the Shields number $A = 9/2\ \eta_f \dot{\gamma}_c / \left(\|\mathbf{g}\|\left(\rho_p - \rho_f\right)L\right)$, the ratio of the densities ρ_p/ρ_f, the reduced particle radius $\tilde{a} = a/L$, and the inverse of the squared Froude number $\tilde{g} = gL/U^2$. However, only 4 parameters are independent since $2/9Re(\rho_p/\rho_f - 1)A\tilde{g} = 1$.

In the case of particle resuspension in an eccentric Couette flow, instead of one single characteristic length, the flow depends on 4 different lengths, namely the inner and outer radii R_{in} and R_{out}, the eccentricity e and the initial height of the sediment h_0. As a consequence, 8 dimensionless numbers may be defined, among which 7 may be varied independently. We chose to compute the following numbers in the case of the two considered experiments:

- $Re = (R_{out} - R_{in})R_{in}\omega\rho_f/\eta_f$ the Reynolds number
- $A = 9/2\eta_f \omega R_{in}/\left(\left(R_{out} - R_{in}\right)g\left(\rho_p - \rho_f\right)h_0\right)$ the Shields number
- $1/\tilde{g} = \omega^2 R_{in}/g$ the squared Froude number
- $a/(R_{out} - R_{in})$ the reduced particle radius that drives the time scale for particle migration in the radial direction
- $\varepsilon = e/(R_{out} - R_{in})$ the reduced eccentricity that drives recirculation
- ρ_p/ρ_f, R_{in}/R_{out}, R_{in}/h_0

In Tables III and IV are displayed the values of all 8 dimensionless numbers in the case of the experiments by D'Ambrosio [63] and Saint-Michel *et al.* [3].

TABLE III. Values of all 8 dimensionless numbers for the experiment by D'Ambrosio, Blanc, and Lemaire [4] (Section IV B).

ε	A	Re	$\frac{\omega^2 R_{in}}{g}$	$\frac{\rho_p}{\rho_f}$	$\frac{a}{R_{out}-R_{in}}$	$\frac{R_{in}}{R_{out}}$	$\frac{R_{in}}{h_0}$
0	1.345	1.86	0.076	1.12	0.0268	0.79	0.89
0.01	1.345	1.86	0.076	1.12	0.0268	0.79	0.89
0.05	1.345	1.86	0.076	1.12	0.0268	0.79	0.89
0.1	1.345	1.86	0.076	1.12	0.0268	0.79	0.89

[1] A. Badia, Y. D'Angelo, F. Peters, and L. Lobry, "Frame-invariant modeling for non-brownian suspension flows," Journal of Non-Newtonian Fluid Mechanics **309**, 104904 (2022).
[2] S. R. Subia, M. S. Ingber, L. A. Mondy, S. A. Altobelli, and A. L. Graham, "Modelling of concentrated suspensions using a continuum constitutive equation," Journal of Fluid Mechanics **373**, 193–219 (1998).

TABLE IV. Values of all 8 dimensionless numbers for the experiment by Saint-Michel *et al.* [3]. (Section IV B)

$\dot{\gamma}\,(s^{-1})$	A	Re	$\frac{\omega^2 R_{in}}{g}$	$\frac{\rho_p}{\rho_f}$	$\frac{a}{R_{out}-R_{in}}$	$\frac{R_{in}}{R_{out}}$	$\frac{R_{in}}{h_0}$	ε
25	0.204	0.45	0.011	2.43	0.0625	0.92	2.61	0.05
50	0.408	0.896	0.044	2.43	0.0625	0.92	2.61	0.05
100	0.816	1.79	0.178	2.43	0.0625	0.92	2.61	0.05
250	2.04	4.48	1.11	2.43	0.0625	0.92	2.61	0.05

[3]B. Saint-Michel, S. Manneville, S. Meeker, G. Ovarlez, and H. Bodiguel, "X-ray radiography of viscous resuspension," Physics of Fluids **31**, 103301 (2019).
[4]E. D'Ambrosio, F. Blanc, and E. Lemaire, "Viscous resuspension of non-brownian particles: determination of the concentration profiles and particle normal stresses," Journal of Fluid Mechanics **911**, A22 (2021).
[5]F. Gadala-Maria, *The rheology of concentrated suspensions*, Ph.D. thesis, Stanford University (1979).
[6]D. Leighton and A. Acrivos, "The shear-induced migration of particles in concentrated suspensions," Journal of Fluid Mechanics **181**, 415–439 (1987).
[7]J. R. Abbott, N. Tetlow, A. L. Graham, S. A. Altobelli, E. Fukushima, L. A. Mondy, and T. S. Stephens, "Experimental observations of particle migration in concentrated suspensions: Couette flow," Journal of Rheology **35**, 773–795 (1991).
[8]A. W. Chow, S. W. Sinton, J. H. Iwamiya, and T. S. Stephens, "Shear-induced particle migration in couette and parallel-plate viscometers: Nmr imaging and stress measurements," Physics of Fluids **6**, 2561–2576 (1994).
[9]R. J. Phillips, R. C. Armstrong, R. A. Brown, A. L. Graham, and J. R. Abbott, "A constitutive equation for concentrated suspensions that accounts for shear-induced particle migration," Physics of Fluids A: Fluid Dynamics **4**, 30–40 (1992).
[10]M. Sarabian, M. Firouznia, B. Metzger, and S. Hormozi, "Fully developed and transient concentration profiles of particulate suspensions sheared in a cylindrical couette cell," Journal of Fluid Mechanics **862**, 659–671 (2019).
[11]Z. Fang and N. Phan-Thien, "Numerical simulation of particle migration in concentrated suspensions by a finite volume method," Journal of Non-Newtonian Fluid Mechanics **58**, 67–81 (1995).
[12]T. Dbouk, E. Lemaire, L. Lobry, and F. Moukalled, "Shear-induced particle migration: Predictions from experimental evaluation of the particle stress tensor," Journal of Non-Newtonian Fluid Mechanics **198**, 78–95 (2013).
[13]O. Ozenda, P. Saramito, and G. Chambon, "Shear-induced migration in concentrated suspensions: particle mass conservation, contact pressure and jamming," Journal of Non-Newtonian Fluid Mechanics **304**, 104805 (2022).
[14]P. R. Nott and J. F. Brady, "Pressure-driven flow of suspensions: simulation and theory," Journal of Fluid Mechanics **275**, 157–199 (1994).
[15]J. F. Morris and F. Boulay, "Curvilinear flows of noncolloidal suspensions: The role of normal stresses," Journal of Rheology **43**, 1213–1237 (1999).
[16]D. Leighton and A. Acrivos, "Viscous resuspension," Chemical Engineering Science **41**, 1377–1384 (1986).
[17]A. Acrivos, R. Mauri, and X. Fan, "Shear-induced resuspension in a couette device," International Journal of Multiphase Flow **19**, 797–802 (1993).
[18]M. M. Denn and J. F. Morris, "Rheology of non-brownian suspensions," Annual review of chemical and biomolecular engineering **5**, 203–228 (2014).
[19]E. Guazzelli and O. Pouliquen, "Rheology of dense granular suspensions," Journal of Fluid Mechanics **852**, P1 (2018).
[20]J. F. Morris, "Toward a fluid mechanics of suspensions," Physical Review Fluids **5**, 110519 (2020).
[21]T. Dbouk, L. Lobry, and E. Lemaire, "Normal stresses in concentrated non-brownian suspensions," Journal of Fluid Mechanics **715**, 239–272 (2013).
[22]R. M. Miller, J. P. Singh, and J. F. Morris, "Suspension flow modeling for general geometries," Chemical Engineering Science **64**, 4597–4610 (2009).
[23]D. Lhuillier, "Migration of rigid particles in non-brownian viscous suspensions," Physics of Fluids **21** (2009).
[24]P. R. Nott, E. Guazzelli, and O. Pouliquen, "The suspension balance model revisited," Physics of Fluids **23** (2011).
[25]R. I. Tanner, "Aspects of non-colloidal suspension rheology," Physics of Fluids **30** (2018).
[26]J. F. Morris, "Progress and challenges in suspension rheology," Rheologica Acta , 1–13 (2023).
[27]I. E. Zarraga, D. A. Hill, and D. T. Leighton, "The characterization of the total stress of concentrated suspensions of noncolloidal spheres in newtonian fluids," Journal of Rheology **44**, 185–220 (2000).
[28]F. Boyer, O. Pouliquen, and É. Guazzelli, "Dense suspensions in rotating-rod flows: normal stresses and particle migration," Journal of Fluid Mechanics **686**, 5–25 (2011).
[29]É. Couturier, F. Boyer, O. Pouliquen, and É. Guazzelli, "Suspensions in a tilted trough: second normal stress difference," Journal of Fluid Mechanics **686**, 26–39 (2011).
[30]F. Qi and R. I. Tanner, "Relative viscosity of bimodal suspensions," Korea-Australia Rheology Journal **23**, 105–111 (2011).
[31]S.-C. Dai, E. Bertevas, F. Qi, and R. I. Tanner, "Viscometric functions for noncolloidal sphere suspensions with newtonian matrices," Journal of Rheology **57**, 493–510 (2013).
[32]S. Dai and R. I. Tanner, "Elongational flows of some non-colloidal suspensions," Rheologica Acta **56**, 63–71 (2017).
[33]A. Vázquez-Quesada, R. I. Tanner, and M. Ellero, "Shear thinning of non-colloidal suspensions," Physical review letters **117**, 108001 (2016).
[34]R. I. Tanner and S. Dai, "Particle roughness and rheology in noncolloidal suspensions," Journal of Rheology **60**, 809–818 (2016).
[35]A. Mahmud, S. Dai, and R. I. Tanner, "A quest for a model of non-colloidal suspensions with newtonian matrices," Rheologica Acta **57**, 29–41 (2018).
[36]O. Ozenda, P. Saramito, and G. Chambon, "A new rate-independent tensorial model for suspensions of noncolloidal rigid particles in newtonian fluids," Journal of Rheology **62**, 889–903 (2018).
[37]O. Ozenda, P. Saramito, and G. Chambon, "Tensorial rheological model for concentrated non-colloidal suspensions: normal stress differences," Journal of Fluid Mechanics **898**, A25 (2020).
[38]J. J. Gillissen, C. Ness, J. D. Peterson, H. J. Wilson, and M. E. Cates, "Constitutive model for time-dependent flows of shear-thickening suspensions," Physical review letters **123**, 214504 (2019).
[39]J. Gillissen, C. Ness, J. D. Peterson, H. J. Wilson, and M. Cates, "Constitutive model for shear-thickening suspensions: Predictions for steady shear with superposed transverse oscillations," Journal of Rheology **64**, 353–365 (2020).
[40]F. Blanc, F. Peters, J. J. Gillissen, M. E. Cates, S. Bosio, C. Benarroche, and R. Mari, "Rheology of dense suspensions under shear rotation," Physical Review Letters **130**, 118202 (2023).
[41]R. I. Tanner and S. Dai, "Forming a composite model for non-brownian suspensions," Physics of Fluids **34** (2022).
[42]A. Deboeuf, G. Gauthier, J. Martin, Y. Yurkovetsky, and J. F. Morris, "Particle pressure in a sheared suspension: A bridge from osmosis to granular dilatancy," Physical review letters **102**, 108301 (2009).
[43]E. D'Ambrosio, F. Blanc, and E. Lemaire, "The characterization of the particle normal stresses of concentrated granular suspensions by local rheometry," Journal of Fluid Mechanics **967**, A34 (2023).
[44]W. Chèvremont, B. Chareyre, and H. Bodiguel, "Normal viscosity and viscous resuspension of non-brownian suspensions," arXiv preprint arXiv:2103.03718 (2021).
[45]G. Bossis, A. Meunier, and J. Sherwood, "Numerical simulations of viscous resuspension," Chemical Engineering Science **47**, 981–991 (1992).
[46]B. Vowinckel, E. Biegert, E. Meiburg, P. Aussillous, and É. Guazzelli, "Rheology of mobile sediment beds sheared by viscous, pressure-driven flows," Journal of Fluid Mechanics **921**, A20 (2021).
[47]G. H. Wannier, "A contribution to the hydrodynamics of lubrication," Quarterly of Applied Mathematics **8**, 1–32 (1950).
[48]B. Ballal and R. Rivlin, "Flow of a newtonian fluid between eccentric rotating cylinders: inertial effects," Archive for Rational Mechanics and Analysis **62**, 237–294 (1976).
[49]P. Swanson and J. Ottino, "A comparative computational and experimental study of chaotic mixing of viscous fluids," Journal of Fluid Mechanics **213**, 227–249 (1990).
[50]N. Phan-Thien, A. L. Graham, S. A. Altobelli, J. R. Abbott, and L. A. Mondy, "Hydrodynamic particle migration in a concentrated suspension undergoing flow between rotating eccentric cylinders," Industrial & engi-

neering chemistry research **34**, 3187–3194 (1995).
[51]R. B. Bird, R. C. Armstrong, and O. Hassager, *Dynamics of polymeric liquids. Vol. 1: Fluid mechanics* (John Wiley and Sons Inc., New York, NY, 1987).
[52]R. I. Tanner, *Engineering rheology*, Vol. 52 (OUP Oxford, 2000).
[53]J. Morris and J. Brady, "Pressure-driven flow of a suspension: Buoyancy effects," International journal of multiphase flow **24**, 105–130 (1998).
[54]S. Gallier, E. Lemaire, F. Peters, and L. Lobry, "Rheology of sheared suspensions of rough frictional particles," Journal of Fluid Mechanics **757**, 514–549 (2014).
[55]F. Peters, G. Ghigliotti, S. Gallier, F. Blanc, E. Lemaire, and L. Lobry, "Rheology of non-brownian suspensions of rough frictional particles under shear reversal: A numerical study," Journal of rheology **60**, 715–732 (2016).
[56]L. Lobry, E. Lemaire, F. Blanc, S. Gallier, and F. Peters, "Shear thinning in non-brownian suspensions explained by variable friction between particles," Journal of Fluid Mechanics **860**, 682–710 (2019).
[57]A. Badia, *Modélisation numérique de suspensions non-browniennes concentrées en écoulement rhéométrique ou général*, Ph.D. thesis, Université Côte d'Azur (2021).
[58]A. E. Larreteguy, L. F. Barceló, and P. A. Caron, "A bounded upwind-downwind semi-discrete scheme for finite volume methods for phase separation problems," Applied Mathematical Modelling **50**, 118–134 (2017).
[59]R. Bürger, A. García, K. Karlsen, and J. Towers, "A family of numerical schemes for kinematic flows with discontinuous flux," Journal of Engineering Mathematics **60**, 387–425 (2008).
[60]E. Guyon, J.-P. Hulin, and L. Petit, *Hydrodynamique physique* (EDP Sciences, 2021).
[61]E. Ryssel and P. Brunn, "Comparison of a quasi-newtonian fluid with a viscoelastic fluid in planar contraction flow," Journal of Non-Newtonian Fluid Mechanics **86**, 309–335 (1999).
[62]M. Orsi, L. Lobry, and F. Peters, "Frame-invariant sub-grid corrections to the fictitious domain method for the simulation of particulate suspensions in nonlinear flows using openfoam," Journal of Computational Physics **474**, 111823 (2023).
[63]E. D'Ambrosio, *Imagery of suspensions to measure particle stresses in non-Brownian suspensions*, Ph.D. thesis, Côte d'Azur University (2020).